END
DATE
FILMED
3 82
DTIC

AD

THE EFFECT OF SIMULATED
WELDING CONDITIONS ON
AUSTENITE DECOMPOSITION KINETICS

by

F.A. CALVO, B.G. MELLOR and A.J. CRIADO

July 1981

United States Army
Research and Standardization
Group (Europe)

London England

United States Air Force
European Office of Aerospace
Research and Development

London England

2 2 1982

A

82 02 22 098

AD

THE EFFECT OF SIMULATED
WELDING CONDITIONS ON
AUSTENITE DECOMPOSITION KINETICS

by

F. A. CALVO, B.G. MELLOR and A.J. CRIADO

July 1981

United States Army
Research and Standardization
Group (Europe)

London England

United States Air Force
European Office of Aerospace
Research and Development

London England

SECURITY CLASSIFICATION OF THIS PAGE (When Data Entered)

REPORT DOCUMENTATION PAGE	READ INSTRUCTIONS BEFORE COMPLETING FORM

1. REPORT NUMBER	2. GOVT ACCESSION NO.	3. RECIPIENT'S CATALOG NUMBER
	AD-A111 189	

4. TITLE (and Subtitle)	5. TYPE OF REPORT & PERIOD COVERED
The Effect of Simulated Welding Conditions on Austenite Decomposition Kinetics	Final Report May 81
	6. PERFORMING ORG. REPORT NUMBER

7. AUTHOR(s)	8. CONTRACT OR GRANT NUMBER(s)
F.A. Calvo, B.G. Mellor and A.J. Criado	DAJA37-80-C-0298

9. PERFORMING ORGANIZATION NAME AND ADDRESS	10. PROGRAM ELEMENT, PROJECT, TASK AREA & WORK UNIT NUMBERS
Universidad Complutense, Madrid, Spain	IT161102BH57-01

11. CONTROLLING OFFICE NAME AND ADDRESS	12. REPORT DATE
USARDSG-UK, Box 65 FPO NY 09510	July 1981
	13. NUMBER OF PAGES
	86

14. MONITORING AGENCY NAME & ADDRESS(If different from Controlling Office)	15. SECURITY CLASS. (of this report)
	Unclassified
	15a. DECLASSIFICATION/DOWNGRADING SCHEDULE

16. DISTRIBUTION STATEMENT (of this Report)

17. DISTRIBUTION STATEMENT (of the abstract entered in Block 20, if different from Report)

Approved for Public Release - Distribution Unlimited

18. SUPPLEMENTARY NOTES

19. KEY WORDS (Continue on reverse side if necessary and identify by block number)

Simulated welding, ferrite to austenite transformation in steels, austenite decomposition in steels, non-equilibrium transformation, continuous cooling transformations, pearlite transformation in steels

20. ABSTRACT (Continue on reverse side if necessary and identify by block number)

The polished surface technique weld simulator has been used to obtain quantitative information on the phase transformations taking place in the weld heat affected zone (HAZ) OF A Fe-0.6C steel. The progress of the ferrite to austenite and austenite to pearlite transformations were determined by quantitative metallography and related to the thermal history, as measured by microthermocouples, throughout the specimen.

DD FORM 1473 EDITION OF 1 NOV 65 IS OBSOLETE
1 JAN 73
S/N 0102-LF-014-6601

20. Continued/

The $\alpha \to \gamma$ transformation is observed to be complete at 780°C under a
heating rate of 50°C s^{-1} while the pearlite in the HAZ coarsens and
dissolves to form an austenite initially inhomogeneous; both these processes
initiate at internal "faults" in the pearlite colonies. On cooling a
pearlitic type morphology with an interlamellar spacing not resolved by
optical microscopy is formed from this austenite.

Inflections were observed in the cooling curves measured in the weld
simulator which did not correspond exactly to the pearlite transformation
temperature at that point but were a reflection of the recalescence effect;
caused by the latent heat evolved by a transformation occurring at some
nearby point. By comparing the weld simulator and continuous cooling
transformation data it was concluded that inhomogeneous austenite favours
the nucleation of a non-conventional pearlite.

The cooling rates between 625°C and 525°C and between 525°C and 425°C were
found to characterize well the fraction of pearlite present in the
microstructure, which due to the rapid cooling experienced does not contain
the equilibrium carbon content.

1. Sumary

The polished surface technique weld simulator has been used to obtain quantitative information on the phase transformations taking place in the weld heat affected zone (HAZ) of a Fe-C 6C steel. The progress of the ferrite to austenite and austenite to pearlite transformations were determined by quantitative metallography and related to the thermal history, as measured by microthermocouples, throughout the specimen.

Te $\alpha \rightarrow \gamma$ transformation is observed to be complete at 780 °C under a heating of 50 °C·s⁻¹ while the pearlite in the HAZ coarsens and dissolves to form an austenite initially inhomogeneous; both these processes initiate at internal "faults" in the pearlite colonies. On cooling a pearlitic type morphology with an interlamellar spacing not resolved by optical microscopy is formed from this austenite.

Inflections were observed in the cooling curves measured in the weld simulator which did not correspond exactly to the pearlite transformation temperature at that point but were a reflection of the recalescence effect, caused by the latent heat evolved by a transformation occurring at some nearby point. By comparing the weld simulator and continuous cooling transformation data it was concluded that inhomogeneous austenite favours the nucleation of a non-conventional pearlite.

The cooling rates between 625 °C and between 525 °C and 425 °C were found to characterize well the fraction of pearlite present in the microstructure, which due to the rapid cooling experienced does not contain the equilibrium carbon content.

3

2. List of Keywords

5

3. Table of Contents.

4. List of illustrations

10

11

5. Body of Report

5.1. Introduction

Welding is, perhaps, the most common process employed to form a permanent joint between metallic components. The process is in essence so simple that it is no wonder it is so widely used. However, this apparent simplicity is deceptive; welding in fact involves more sciences and variables than many other industrial processes, which may explain why most of those concerned are satisfied with a very crude understanding of its complications. In fusion welding, for example, the molten metal heats up the solid metal in contact with it, thus establishing a temperature gradient in the material being welded. The temperatures in the metal range from above the melting point of the material to room temperature in parts not too *distant from the weld. It will suffice to remember* the various phenomena that are strongly dependent on temperature to realize the potential enormous complexity of the so called heat affected zone (HAZ). These phenomena include allotropic changes *in the metal, variations of the mutual solubility of* the distinct phases, the processes of recovery, polygonization, recrystallization ad grain growth, the disappearance of carefully prepared structures and their replacement by others perhaps intentionally avoided, plastic deformations resulting from thermal stresses, residual stresses caused by both volume changes and by the expansion and contraction of the material constrained by the solid material not heated etc. That is, welding will influence *all those properties which are affected by heat* treatments. The heat treatment variables introduced by welding are.

1) rate of heating

2) maximum temperature reached.

3) time at this temperature.

4) cooling rate.

The microstructure — the nature, shape, dimension and distribution of the phases present in the material will be determined by the thermal history of the specimen and this, in turn, will determine the properties of the material. For this reason it is so important to observe and understand how and why materials transform on welding.

In any systematic investigation of the heat affected zone it must be possible to relate a given microstructure to its thermal history. In order to reduce the number of variables introduced in the process and to standardize the test conditions more easily, over the last twenty-five years welding simulators (1-18) have been constructes which are capable of applying a previously programmed and repeatable thermal cycle to the material being examined similar to that experienced in welding. While these types of experiments do not provide results which can be used in a fully quantitative sense for design purposes they can be sufficiently valid to allow qualitative trends to be firmly established.

Most of these welding or HAZ simulators employ direct resistance heating of the specimen, although recently high frequency induction heating has been employed principally because of the versatility afforded by this method of heating (5).

However, the thermal cycles generated by these complex simulators do not, in generak, reproduce the very high heating rate developed in welding (19), and in view of this major limitation it was thought that a better and much simpler technique to reproduce welding cycles would be to use an argon-tungsten arc welding torch as the heat source. In this technique a flat specimen is heated on one side by this arc while observations fo the microstructural changes are made on the other side. This method has various advantages:

1) The thermal cycles applied can be varied over a considerable range of heating and cooling rates while the maximum temperature can be set at any desired value.

2) By spot welding microthermocouples at different points on the surface of the specimen the thermal cycle producing a given microstructure can be accurately recorded.

3) The observation surface can be polished before the arc is struck. This enables the comparison of structures before and after welding on the same areas without the necessity of repolishing, thus allowing any surface effects resulting from the phase changes, or from stresses developed during the weld simulation, to be studied without their possible masking or elimination in a subsequent polish (Polish Surface Technique, PST).

4) The apparatus used is simpler and reproduces more closely the thermal cycles in welding than a conventional thermal simulator apparatus.

This welding simulation technique has been used by Calvo and coworkers (20-22) to study the transformations taking place during the welding of low carbon steels, tough pitch copper, deoxidized copper, brass, aluminium bronzes and commercial purity aluminium.

However this technique, to date, has only been used to obtain qualitative microstructural information on the transformations occurring in the HAZ by using principally optical metallography, but also, to a lesser extent, both transmission and Scanning electron metallography.

It was thus thought desirable to extend the technique and attempt to quantify the changes taking place in the HAZ, using quantitative metallography to determine the fraction of the phases present, and microthermocouples to determine the thermal history responsible for those changes and so proportion fundamental structure/thermal history relationships which could be of use for predicting the properties of actual welds.

In welding, and in the PST weld simulator not only does the temperature vary with time (in both heating and cooling cycles) but also a steep temperature gradient will exist in the specimen. That is, the transformation conditions will not correspond to either isothermal or continuous cooling conditions. In addition the standard isothermal or continuous cooling transformations are determined after an austenitization treatment, which is at a sufficiently high temperature or for a sufficiently long time, so as to decompose completely the phases previously present and eliminate any carbon or alloy element concentration gradients. However, in a weld, and in the PST weld simulation, the time the specimen is above the eutectoid temperature is of the order of seconds, and thus in some regions of the HAZ the austenite has not time to become homogeneous before transforming on cooling.

It is well known (23-25) that continuous cooling displaces the initiation of the pearlite eutectoid reaction to longer times than in isothermal heat treatments and suppresses the nose of the transformation curve to lower temperatures. The maximum temperature reached during the welding cycle is reported (26) to affect the subsequent transformation of the austenite on cooling, an increase in temperature and duration of the austenitizing treatment intensifying the decomposition of the austenite. The presence of a temperature gradient is known to affect substantially the thermal stability and transformation characteristics of a particular microstructure (27-30), and in particular it has been reported that the nucleation of pearlite in a temperature gradient during isovelocity growth is slower than that under continuous or isothermal transformation conditions (31). It seems evident that when transformations take place under different conditions the nucleation kinetics of the different phases are different although in general (31) the growth kinetics, interlamellar spacing of the pearlite are independent of the transormation mode (23,31) depending only on the temperature of transformation which, in welding, varies with the time.

In view of the complexity of the transformations a step-by-step comparative approach was considered necessary using continuous cooling transformation (CCT) data together with data provided by the PST welding simulator. The steel chosen for study was of nominal composition Fe-O.6C,

14

thus enabling both the pearlite reaction and the pro-eutectoid ferrite reaction to be studied in the same specimens.

5.2. Experimental

5.2.1. PST weld simulator

In view of the necessity of obtaining quantitative information from the weld simulation tests it was felt that an improved welding chamber and device to locate the tungsten electrode at a precise position over the specimen should be constructed. Figure 1 shows the chamber now used for weld simulation which basically consists of a copper water-cooled chamber with a stainless steel insert into which the cylindrical specimens 25 mm in diameter and 2 − 6 mm thick are placed. The chamber is thus sealed by the specimen which has its prepared surface inside the chamber. In the previous chamber the specimens were in the shape of a truncated cone which, although ensuring a satisfactory fit between the stainless steel insert and the specimen during the welding cycle, required careful machining to match the taper angle of the specimen to that of the insert. The specimen, its edges previously covered with aluminium foil, is loaded into the insert by applying pressure from a hydraulic press. This technique thus ensures a perfect fit between specimen and stage. After insertion the surplus aluminium foil is removed and when the thermo-couples have been connected (section 7.2.4.) the chamber is assembled.

The tungsten welding electrode is positioned over the exterior specimen face and aligned with it by means of a cross scribed on the specimen to mark its centre (Figure 2). The distance between the specimen surface and the electrode is adjusted by a micrometer screw device incorporated into the electrode assembly.

As in the previous chamber, the prepared surface of the specimen in the interior of the chamber is protected against oxidation during the test by passing a flow of 20 ft^3h^{-1} of argon continuously over the surface. An overall view of the equipment is shown in Figure 3.

5.2.2. Specimens

5.2.2. (a) Heat treatment.

Specimens of approximate composition Fe-0.6C were austenitized for 15 minutes at 1000°C and then maintained for 3.2 h at 712°C and subsequently left to cool in the furnace. Both the austenitization and the subsequent heat treatment below the eutectoid temperature were performed in an Edwards Series 1200 Vacuum furnace the vacuum during the process being 10^{-5} torr.

This isothermal heat treatment was designed to produce a specimen with a relatively large pearlite interlamellar spacing so enabling the pearlite formed from the austenite during the weld cycle to be easily distinguisable from the original microstructure. However the nature of the equipment used made the cooling rate from 1000°C to the lower transformation temperature relatively slow which le to the production of a rather coarse ferrite.

5.2.2. (b) Specimen preparation.

In the experiments realized the thickness of the specimens (one of the variables) was fixed at 3 and 4 mm. Both of the faces of the specimens were ground on emery papers to 600 grade. On one face the centre was marked while on the other a diameter was scribed. On this diameter small marks were scribed at various distances from the border of the specimn which served to indicate the positions to spot weld the three microthermocouples. These distances, based on experience, were chosen to be in and around the HAZ.

5.2.3. Thermocouple preparation

Chromel-alumel microthermocouples were prepared from wires of 0.01 mm diameter by spot welding by condenser discharge. The preparation conditions for joining the wire were 125 V condenser charging voltage and 25 mF capacity. The thermocouples were examined after preparation by a low power optical microscope and only ones with a small spherical junction were selected for subsequent welding to the specimen.

The microthermocouples prepared as previously described were spot welded by condenser discharge at the positions previously marked on the specimen; the thermocouple being accurately located at the marks by means of a low power microscope. The welding conditions were: charging voltage 125 V, and 10 mF capacity. After welding the thermocouple junction was examined by low power optical microscopy and the weld between the specimen and thermocouple checked by a simple mechanical test.

After welding the two or three thermocouples to the surface of the specimens, the distances of the thermocouples from the edge of the specimen were carefully measured by a travelling microscope.

5.2.4. PST weld simulation test.

The specimens with thermocouples attached were mounted in the weld simulator by the method described in section 7.2.1. and the thermocouple wires soft soldered to terminals in the interior of the chamber. The terminals, led to the exterior of the chamber, were connected by screened cables to three recorders a Honeywell Brown Electronik recorder (chart speed 25.4 mm/s), a Leeds and Northrup Speedomax (chart speed 5.8 mm/s) and a Linseis TYP 2041 recorder (chart speeds upto 50 mm/s.

Once the chamber was assembled (section 7.2) the conditions of the test were selected. These were, argon flow 20 $ft^3 h^{-1}$, distance between specimen and welding electrode, 2 mm, welding intensity 105A, welding voltage 21 V, duration of the test 10s. The arc Was struck by superimposing a high frequency current.

5.3. Results

5.3.1. Thermal history.

Figure 4 shows a typical temperature-time curve constructed from the curves registered on the recorders. The curves were in general quite smooth but some small abnormal regions or inflections (Fig. 4b) were observed on the cooling part of the curve. The temperatures at which these inflections occurred were determined (T_1 and T_2).

From various experiments with thermocouples positioned at different points on the specimen the centre of the fusion zone was established. This information is presented in the following graphs.

Figures 5 and 6 show the temperature reached at different times during the heating cycle (t = 3, 5, 7, 9, 10 s) as a function of distance from the centre of the fusion zone for specimens 3 and 4 mm thick.

Figures 7 and 8 show the temperature reached at different times during the cooling cycle (t = 11, 13, 15, 17, 19 s) as a function of distance from the centre of the fusion zone for specimens 3 and 4 mm thick.

Figures 9 and 10 show the heating rate within various temperature intervals as a function of distance from the centre of the fusion zone for specimens 3 and 4 mm thick.

Figures 11 and 12 show the cooling rate within various temperature intervals as a function of distance from the centre of the fusion zone for specimens 3 and 4 mm thick.

In addition to these general representations of the thermal history of the specimens during the weld cycle the following additional graphs can be drawn.

Figures 13 and 14 show the maximum temperature reached as a function of distance from the centre of the fusion zone for specimens 3 and 4 mm thick.

Figures 15 and 16 show the time above 725°C (approximately the eutectoid temperature) and above 825°C as a function of distance from the centre of the fusion zone for the 3 and 4 mm thick specimens.

Figures 17 and 18 show the maximum temperature reached as a function of time above 725°C for specimens of 3 and 4 mm thickness.

Figures 19 and 20 show the temperature corresponding to the start, T_1, and finish, T_2, of the inflection in the cooling curves as a function of distance from the centre of the fusion zone for the 3 and 4 mm thick specimens.

5.3.2. Qualitative Metallographic observations.

5.3.2. (a) Optical microscopy.

After the test specimen was taken from the chamber and observed under a low power optical microscope. In some tests the arc was observed not to have struck in the precise centre of the specimen and so the fusion zone although circular was not symmetrical about the geometric centre. To determine the centre of the fusion zone and so refer the thermocouple distances to that and not to the geometric centre of the specimen photomacrographs were taken. The centre of the fusion zone was then obtained by geometric construction and the thermocouple distances measured with respect to this centre.

The thermocouples were then removed and that face polished, etched with nital to reveal the overall appearance of the specimen and observed microscopically. A modified nital etch consisting of nital plus one tenth of its volume of 4% picral was found useful in differentiating between austenite, martensite and fine pearlite.

Figure 21 shows at low magnification the general aspects of the material prior to weld simulation. As can be seen proeutectoid ferrite is the continuous phase surrounding pearlite colonies which may include small ferrite particles. Figure 22, at higher magnifications, shows the typical pearlitic structure.

Figure 23 shows a macrograph of a specimen, etched after weld simulation. The fusion and HAZ are seem to be circular and perfectly defined. At higher magnifications the region close to the fusion zone was observed to have a martensitic structure in which some black etching nodules (Figure 24) were distributed in grain boundaries and internally. The proportion of these nodules increased in regions closer to the non affected zone as seen in Figure 25.

At the border of the HAZ with the non-affected region the ferrite to austenite transformation was observed to start, Figures 26 and 27. The ferrite boundaries become irregular with many indentations while the original pearlite grains now etch irregularly and their microstructure is not resolved at optical magnifications. Regions of "martensite" are observed in the interior of some of these grains.

The proportion of ferrite is observed to decrease towards the fusion zone. The ferrite outlining the grain boundaries becomes very irregular and highly indented (Figure 28).

5.3.2. (b) Scanning Electron Microscopy (SEM)

A JEOL JSM-35C Scanning Electron Microscope (SEM) was used to examine the HAZ at higher magnifications in specimens subjected to weld simulation. Prior to observation in the SEM the specimens were deeply etched by employing either nital or the modified nital etch referred to in section 7.3.2. (a). Some specimens were demagnetised by placing them in a coil through which an alternate current was passed. This current was slowly reduced to zero and the specimens once removed from the coil were then immediately inserted into the SEM.

Figure 29 shows the structure of ferrite and pearlite in a region of the non-affected zone very close to the border with the HAZ. The boundary of the ferrites is observed to be regular and the pearlite colonies contain many lamellar terminations and faults.

In regions close to the fusion zone (Figure 30) martensite was the predominant microstructure. However in regions closer to the non-affected region, nodules of pearlite with a very fine interlamellar spacing (~0.12 μm) were observed (Figure 31). These nodules are the black etching areas not resolved by optical microscopy shown in Figure 24 and 25. In Figure 31 regions with an apparent bainitic morphology are also observed to have nucleated from the opposite side of a prior austenite grain boundary to which "pearlite" has nucleated.

17

Further towards the non-affected zone the proportion of these "pearlite" nodules increases (Figure 32) and they are seen to have grown from the grain boundaries of the prior austenite grain, the centre of which has transformed to martensite.

Yet closer to the non-affected zone the microstructure is more irregular (Figures 33 and 34), but the structure is still predominantly pearlitic and martensitic. However the "pearlite" is observed to be rather irregular in morphology.

Still closer to the non-affected zone the microstructure becomes very complex, Figures 35 and 36. Regions of partial dissolution of the pearlite areseen while on the left of Figure 36, corresponding to a region closer to the fusion zone, small nodules of pearlite with a very fine interlamellar spacing (easily distinguishable from the original pearlite structure which has a larger interlamellar spacing, 0.35 um) can be discerned.

Figure 37 corresponding to a region in the HAZ at the boundary with the non-affected zone shows initiation of the pearlite/ferrite dissolution processes. The ferrite boundaries have become indented and very irregular and in some cases are surrounded by a "halo" with a structure not resolved. The pearlite is observed to have become more irregular and has a similar appearance to pearlite during the early stages of a coarsening reaction (32, 33). Some pearlite colonies are noted to have reacted to a greater degree. Figure 38 shows, at higher magnifications, details of the decomposition of the pearlite.

SEM was also employed to carry out a preliminary study on the effect prior specimen microstructure has on the microstructures formed during weld simulation. A specimen with a normalized microstructure was subjected to weld simulation using the conditions described in section 7.2.4., but with a time of 4s. After this treatment the specimen was given a final polish, etched in 7% nital for 6 min and observed in the SEM.

Figure 39 shows, at low magnification, the boundary ot the non-affected zone (to the right) with the HAZ. As can be appreciated this boundary is abrupt and well defined. The ferrite particles in transformation to austenite are observed to be

surrounded by a lighter etching region.

Figure 40 shows, again at a low magnification a region of the HAZ in which the ferrite to austenite transformation has almost reached completion. However ligher etching regions similar in size to the original ferrite particles are still observed in regions where the ferrite has transformed to austenite suggesting that diffusion has not been sufficient to level out carbon concentration gradients associated with this transformation.

Figure 41, a region of Figure 39, at a higher magnification shows a ferrite particle in the process of transforming to austenite. The right hand side of the particle has not begun to react (this side has been to a slighty lower temperature than the left hand side) whereas the left hand boundary has initiated the transformation. Cementite particles are observed to be present at the reacting boundary of the ferrite particle, while what is apparently a fine precipitate is also seen in the proeutectoid ferrite. Non-resolved, light etching areas exist at some ferrite boundaries. The original normalized structure, on the right of Figure 41 is seen to consist of a very irregular carbide despersion.

At a higher magnification, Figure 42 the finner details of the pearlite to austenite transformation can be appreciated. Faults and branching of the lamellae are apparent as is a localised coarsening of the lamellae. Around the ferrite particle the structure is again not well resolved.

In regions closer to the end of the ferrite to austenite transformation the microstructure is more complex and it is difficult to give conventional names to the reaction products, Figure 43 shows, at a higher magnification a region of Figure 40. The region around the ferrite particle is again not resolved and the carbide distribution is very irregular and difficult to interpret. Figure 44 shows carbide morphologies at a grain boundary.

Deep etching using picral was also tried in an attempt to resolve some of the structures not well defined on etching with nital. The etching conditions were 15 min in a 4% picral solution.

Figure 45 shows a pearlite colony at the boundary tetween the non-affected region and the HAZ. The

18

ferrite constituent of the pearlite and the proeutectoid ferrite have been completely dissolved by this etch to reveal well the three dimensional appearance of this microstructure.

Figure 46 indicates a ferrite particle in transformation. Its boundaries have become irregular and appear to be again surrounded by a white etching phase which in some points protrubes into the ferrite particle.

Figure 47 shows details of a pearlite colony in a region just out of the HAZ. The deep etching conditions used has disolved out the ferrite constituent of the pearlite microstructure completely and has caused the cementite lamellae, as they are now unsupported to fall against each other, thus giving rise to a deformed microstructure. Thus some care must be taken when interpretting microstructures after deep etching.

From the results obtained it is believed that a systematic work on the development of proper reagents and etch conditions should be carried out. The SEM requires modified or even new experimental techniques to reveal the microstructures. A new metallography will develop where the old named structure will acquire a more appropiate signicance.

5.3.3. Quantitative optical metallography.
5.3.3. (a) Ferrite.

The percentage of ferrite as a function of distance from the centre of the fusion zone was determined at a magnification of x800 on specimens etched with nital by measuring the fraction of a random line occupied by ferrite. The exact procedure was the following:

The specimen was positioned with the scribed diameter parallel to one of the axis of movement of the stage of a Nikon microscope and the positions of the thermocouples, which served as reference points for the measurements were related to the x, y coordinates of the stage.

Measurements were taken every 0.1 mm along 4 imaginary lines 0.15 mm apart traced parallel and on either side of the scribed diameter. At

every field selected ten measurements were made by rotating the measuring line of the graticule through 18". At each position of the graticule the fraction of the line occupied by ferrite was determined. The value for the fraction occuppied by ferrite at a given distance from the centre of the fusion zone was calculated by averaging the 40 measurements taken (10 measurements on 4 traverses). The standard deviation and 95% confidence limits for these average values were also determined. Figures 48 and 49 show histograms constructed from these data and represent the percentage of ferrite as a function of distance from the centre of the fusion zone for specimens 3 and 4 mm thick.

Figures 40 and show the percentage of ferrite with the 95% confidence limits for these values as a function of distance from the centre of the fusion zone for 3 and 4 mm specimens. The results for the measurements of pearlite (section 7.3.3. (b) are also given).

5.3.3. (b) Austenite decomposition product.

As shown in Figures 24 and 25 the principal decomposition products of the austenite formed from pearlite and ferrite during the weld cycle, are martensite and what at optical magnifications appears to be pearlite of a very fine spacing. Some bainite and ferrite were also observed. Figures 31 and 32 show these nodules as observed by SEM confirming the lamellar morphology. The percentage of fine pearlite as a function of distance from the centre of the fusion zone was determined by using the same technique as that described for ferrite in section 7.3.3. (a), but the picral modified etch was used. At above approximately 50% transformed it was very difficult to masure the fraction accurately.

Figures 52 and show the histograms of fraction transformed to pearlite as a function of distance from the centre of the fusion zone for specimens 3 and 4 mm thick. Figures 50 and 51 show, together with the ferrite results, the pearlite fraction with 95% confidence limits as a function of distance from the centre of the fusion zone for 3 and 4 mm specimens.

19

5.4. Continuous cooling transformation data

5.4.1. Introduction.

As one of the aims of this work was to compare the results obtained in the PST weld simulator with those obtained under conventional conditions, the possession of conventional data refering to this steels is essential. Owing to the fact that the presence of impurities and minor elements in steels is known to substantially affect the transformation kinetics it was thought wiser to determine experimentally these conventional data rather than obtain them from the literature. Thus any difference observed between PST weld simulation and conventional results could be attributed to the different thermal conditions of the tests and effects caused by the influence of impurity levels on kinetics eliminated.

Originally it was thought that it would be necessary to determine the transformation kinetics under isothermal (TTT) and continuous cooling conditions (CCT) but in view of the closer approximation of the welding conditions to continuous cooling rather than isothermal conditions, the determination of of only the CCT data was considered suffice.

5.4.2. Experimental.

Specimens of approximate dimensions $3 \times 3 \times 2$ mm were cut from the same specimens as those used in PST weld simulation. A 0.5 mm thick chromel-alumel-thermocouple was spot welded to the specimen and connected to a Linseis TYP 2041 recorder. The specimen heating curve was determined by placing it in a furnace at 1000"C Through which a flow of argon was maintained to prevent decarbunization of the specimen. The specimen was permitted to reach 1000"C after which the specimen was removed from the furnace and allowed to cool in air, the temperature of the specimen being continuously recorded. Any desired cooling rate could be achieved by varying the quenching conditions. The average time the specimen was above 725"C was ~ 45 s.

The grain size of the specimens treated in the manner described was determined by metallographically measuring the average number of grain boundary intercepts per unit length of a random line.

5.4.3. Results.

The grain size determined by the mean linear intercept method was ~ 50μm. Figure 54 shows the start of the reaction at a high cooling rate obtained by partially transforming a specimen. Nodules are observed to have nucleated at some of the austenite grain boundaries.

Figure 55 gives the heating curve which shows an inflection caused by the dissolution of the pearlite and indicates that under a heating rate of 18"C s⁻¹ this transformation takes place at 797 ± 2"C. Figure 56 shows the inflection in the cooling curve produced by the evolution of the latent heat of the eutectoid reaction. As shown in this figure at relatively low cooling rates and higher transformation temperatures a very well defined minimum and maximum temperature were found whereas at higher cooling rates no maximum temperature was detected. In order to determine a characteristic temperature for the reaction by a standard procedure irrespective of cooling rate the following method was adopted. A tangent was drawn to the cooling curve in the region immediately below the transformation and a line was drawn parallel to it such that it was also a tangent to the cooling curve in the region immediately above the inflection. The point of interception of this tangent with the cooling curve was taken as characteristic of the reaction temperature, T_x, at this cooling rate. Figure 56 also shows this construction. As the cooling rate falls off with decreasing temperature this construction will probably give a slightly lower value for the temperature for the start of the reaction than is really the case, but the construction has the advantage that it is easily reproducible irrespective of cooling rate, whereas to estimate directly the first deviation from the cooling curve and take this as the temperature for the initiation fo the reaction is associated with considerable error.

Figure 57 shows several of the experimentally determined cooling curves drawn on the same graph, on which the T_A Temperatures are marked and the time for the initiation of the pearlite reaction as a function of temperature is outlined. Figure 58 shows the transformation temperature, T_A, plotted against t, where t, is the time taken for the specimen to cool from 725°C to the T_A temperature.

From the recorder traces the time taken for the temperature to fall from 725° C to 625°C, from 625°C to 525°C and from 725 to T_A were also determined and Figure 59 shows the transformation temperature T_A plotted as a function of the cooling rates determined from these data.

5.5. Discussion of weld simulation and continuous cooling results.

5.5.1. Metallography.

As seen from both the optical and SEM studies the dissolution of the ferrite is observed to initiate at the boundaries of the ferrite and the pearlite. These boundaries rapidly become very irregular and indented and this dissolution of the ferrite will locally give rise to an austenite with a very low carbon content which with time will tend to form a homogeneous solid solution with the austenite formed from the dissolution of the pearlite. On cooling this area, which inregions close to the border of the HAZ with the non-affected zone will not be homogeneous with respect to carbon concentrations (section 7.5.2. (a)) it is postulated the undissolved or partially dissolved cementite particles will act as nucleations sites for pearlite, thus accounting for the nodules of pearlite found surrounding the partially dissolved ferrite seen in Figures 27 and 28.

The changes in the pearlite structure are observedto start internally in the pearlite colony, preferentially at lamellar faults and terminations in the original pearlite colony. A similar coarsening behaviour has been noted in many lamellar structures, both eutectic and eutectoid (32, 33) and attributed to the coarsening reaction proceeding through a fault migration mechanism. It is also

thought that the coarsening rate in the PST weld simulator is somewhat higher than in isothermal studies which is in agreement with the fact that coarsening in a temperature gradient (in this case of 55°C mm⁻¹) is known to accelerate the coarsening reaction (28, 29, 30).

The dissolution of the pearlite proceeds to give rise to a region of *non-homogeneous* austenite in the centre of the original pearlite colony. This austenitic region will have a carbon concentration of approximately 0.8, i.e. higher than the overall carbon content of the specimen and on cooling will, at the cooling rates in question, form pearlite of a very fine spacing and / or martensite.

In regions closer to the fusion zone the pearlite dissolution reaction proceeds to completion and the austenite becomes more homogeneous and its carbon concentration approaches that of the global carbon concentration in the steel (0.6). On cooling nodules of pearlite with a fine interlamellar spacing are again formed. Other carbide morphologies are also visible which might be described as "bainitic", reflecting the fact that the nature of the decomposition of the austenite is a function of the ease of nucleation and growth of the different carbide/ferrite morphologies which are influenced by local orientation relationships between the austenite and the ferrite/ carbide nucleus and, possibly, the superimposed internal stresses.

In all of the HAZ very little acicular ferrite which might have been expected to be formed on cooling, was observed. However at the cooling rates used in this study the transformation temperatures are low enough so as to make a composition of 0.6 C fall within the lines of the Hultgren extrapolation of the Fe-C equilibrium diagram thus accounting for the non-appearance of ferrite.

5.5.2. Transformation Kinetics.

5.5.2. (a) Ferrite to austenite transformation.

By correlating the results shown in Figures 48-51 which give the regions of the specimens in which the ferrite dissolution reaction is taking place, with Figures 5,6,9,10,13-16, which indicate

the thermal history of the specimens at the same distances, the information given in Table I is obtained. As can be seen the low temperature border of the $\alpha \rightarrow \gamma$ reaction corresponds quite closely to the eutectoid temperature, while the high temperature border is some 20 to 25" above the temperature at which the transformation of ferrite to austenite is completed under equilibrium conditions, (Ae$_1$ = 755"C). It should be borne in mind that the time spent above 725"C includes both the time spent on heating from 725°C to the maximum temperature and also the time spent in cooling from the maximum temperature to 725"C.

To compare these results with those obtained under continuous heating conditions requires the determination of the latter data at heating rates similar to those used in the weld simulator (50"s^{-1} in this temperature interval). As noted in Section 7.4.3. the heating rates experimentally available for determining these data reached only 18°C s^{-1} and, thus without designing and constructing a more specialised piece of equipment, which was outside the scope of this contract, these comparative data cannot be obtained. The same arguments as those put forward in Section 7.4.1. prevent this information from being obtained, with the desired precision, from the literature.

5.5.2. (b) The austenite to pearlite transformation.

Table II is the result of correlating the data given in Figures 50-53 which give the regions of the specimens in which the austenite to pearlite reaction is taking place with Figures 7, 8, 11-16, which indicate the thermal history of the specimens at the same distances. The region of the specimens where the austenite partially transforms to pearlite corresponds to a zone which has been between 4 and 10s, approximately, above 725"C and has reached a maximum temperature of between 810"C and 1150"C. It is quite probable therefore that, especially close to the lower temperature border the austenite from which the pearlite formed was not completely homogeneous both with respect to the total dissolution of the cementite and also to the presence of carbon concentration gradients. In this aspect it is interesting to note that under isothermal conditions (34)

more than 200s at 850"C are necessary to form a homogeneous austenite. However as this process of producing a homogeneous austenite will depend on the value of the diffusion coefficient which increases exponentially with temperature, the degree of homogeneity should also increase rapidly with temperature and the austenite closer to the higher temperature border of this region should be completely homogeneous. As stated in section 7.3.3. (b) the measurement of the fraction of pearlite formed at above 50% pearlite was very difficult. This is thought to be due to overlapping nodules but also it is suspected that the absence of homogeneity of the austenite in this regions which has reached a maximum temperature of 850"C and 825"C and times of 4.8 and 5.3s above 725"C for the 3 and 4 mm thick specimen is giving rise to the presence of non-typical pearlitic structures.

The continuous heating results indicated that with a heating rate of 18°C s^{-1} the pearlite to austenite transformation started at ~ 797"C, 2.4s after passing 725"C. The heating rate used in the weld simulator studies was considerably higher, between 60 — 120°C s^{-1} for the 3 mm thick specimens and between 60-105°C s^{-1} for the 4 mm specimens which wouls suggest that the temperature of the pearlite to austenite transformation should be at a higher temperature. Although attempts were made to detect an inflection in the heating curve abtained in the weld simulator at temperatures of above 725"C, no conclusive indication for the transformation could be detected which, it is felt, was partially due to small oscillations in the arc current intensity affecting the heating rates slightly which, thus perhaps hid any inflections in the heating curve caused by the pearlite to austenite transformation.

However both optical and SEM revealed a change in the morphology of the pearlite adjacent to the boundary of the HAZ and the non-affected zone i.e. at temperatures just slightly above 725"C suggesting that the pearlite to austenite transformation might occur with more rapid kinetics in the weld simulator than under continuous heating conditions.

On cooling this austenite –formed from the pearlite and ferrite– below the eutectoid temperature it will transform to pearlite at a certain under-

cooling. As shown in Figure 4b an inflection was observed in the cooling curves which started at approximately 600°C and finished at approximately 440°C. Figures 19 and 20 show the temperature of the start and finish of this inflection plotted as a function of distance from the centre of the fusion zone. As can be seen there is very little variation of the two temperatures with distance. The higher temperatures, T_1, for both the 3 and 4 mm specimens are very similar but it appears that the lower temperature, T_2, are slightly higher for the 3 mm thick specimens than for the 4 mm ones.

By using the experimentally determined continuous cooling curves for this steel, the temperature at which the steel "ought to" transform in the weld simulator if it were just under continuous cooling conditions can be established. Figures 60 and 61 show several of the cooling curves determined during weld simulation superimposed on the graph showing the start of the pearlite reaction under continuous cooling conditions. The temperature at the point of intersection of the weld simulator cooling curves and the curve corresponding to the initiation of the pearlite reaction (T_x) were read off and are shown in Figures 19 and 20 together with the T_1 and T_2 temperatures as a function of distance from the centre of the fusion zone. As can be appreciated, in all cases, the T_x temperature lies between the upper, T_1, and lower T_2, temperatures determined from the weld simulator cooling curves, and that the T_x temperature increases with distance from the centre of the fusion zone.

Let us now consider in detail the course of the austenite to pearlite decomposition in the weld simulator by postulating that the transformation under simulated welding conditions is identical to that under continuous cooling conditions. When the region in the 3 mm thick specimens which finally has a structure of 50% pearlite at 6.2 mm from the centre of the fusion zone starts to transform at about $520_{\circ}C$ (T temperature) a region which finally has a structure of ~ 8% pearlite at 4.6. mm from the centre of the fusion zone will be at approximately 600°C (Figure 7). This region at 6.2 mm from the centre of the fusion zone, on transforming, will evolve latent heat of the transformation and this latent heat is thought to give rise to a local increase in the temperature (recales-

cence effect) which causes the thermal gradient throughout the specimen to change, and, as the thermal gradient largely determines the cooling rate, a change in the cooling rate will be detected. As an inflection in the cooling rate is what is taken as the T_1 and T_2 temperatures it can be seen from these considerations that although an inflection in the cooling rate at 4.6 mm from the centre of the fusion zone is detected at 600°C, that does not necessarily mean that a transformation at that point starts at 600°C.

Similarly when a point 4.6 mm from the centre of the fusion zone is postulated to start to transform at 490°C (T_x temperature), a point 6.2 mm from the centre of the fusion zone is now at 440°C. When this region around 4.6 mm from the centre of the fusion zone, which is the last region to partially transform to pearlite, finishes transforming (this region has only 8% pearlite and the temperature it finishes transforming is postulated to be only slightly below that at which it started) the absence of evolution of latent heat will reflect itself not only at that point but also at other points, implying that the inflection detected at 440°C at at a point 6.2. mm from the centre of the fusion zone does not necessarily correspond to the end of the transformation at that point.

Thus the inflections detected in the cooling curves determined from the weld simulation test correspond to the outer limits for the transformation of all the material within the transformation region. However, it might be expected that in the region which transform first (closer to the non-affected region) the inflection in the weld cooling curve (T_1) and the predicted transformation temperature (T_x) from the continuous cooling results should agree. The fact that they do not agree exactly but are seen to be approaching coincidence in the region nearest to the non-affected zone, suggests that in this region the transformation is actually occurring at a higher temperature than that predicted from the continuous cooling curves.

A similar behaviour is also observed for the 4 mm thick specimens although the transformation temperatures estimated from the continuous cooling data (T_x) are seen to lie closer to the T_2 temperature than for the 3 mm specimens. Perhaps the larger volume of material transforming (33%

more than for the 3 mm thick specimens) gives rise to a greater local recalescence effect, making T_1 higher.

However from both the 3 mm and 4 mm thick specimens, it is suspected that at least in the region closest to the border of the HAZ with the non-affected material the austenite is decomposing at a higher temperature than that predicted from the continuous cooling results. It is thus postulated that the presence of inhomogeneites favours the nucleation of pearlite. A similar result was found by Hull and Mehl (35, 36) in isothermal studies.

The regions in the specimen at which pearlite occurs are obviously related to the cooling rates in the specimen. By correlating Figures 50-53 which indicate the fraction of pearlite formed as a function of distance from the centre of the fusion zone with Figures 11 and 12 which give the cooling rates within various temperature intervals as a function of distance, Figure 62 is obtained which expresses the fraction of pearlite found as a function of cooling rate within various temperature intervals for specimens 3 and 4 mm thick. It is noted that only the relationship between the cooling rate between 525 and 425"C, ad to a lesser extent that between 625 and 525"C and the fraction of pearlite transformed are the same for both thicknesses of specimen which suggests that these are the most critical temperature intervals for the nucleation of pearlite. This interval contains, according to the continuous cooling data, the pearlite start temperature under the cooling rates present in the weld simulation test. From Figure 62, it can be seen that pearlite is not formed at cooling rates of above approximately 53"C s^{-1} (measured in the 625 to 525"C temperature interval) in the weld simulation test. The continuous cooling data presented in Figure 59 indicate a cooling rate of 55"C s^{-1} in the 625 5o 525"C interval as the maximum for the formation of pearlite, which is thus in good agreement with the weld simulator from an austenite which has reached 1150"C and so is expected to be homogeneous. Thus it is suspected that when the austenite is homogeneous, the transformations in the weld simulator can essentially be described by continuous cooling data.

Figures 50 and 52 showed that in the 3 mm

thick specimen there existed a region between 4.6 and 5.6 mm from the centre of the fusion zone which had about 13% pearlite, whereas in the 4 mm specimens (Figures 51 and 53) the proportion of pearlite falls off more rapidly. On a close examination of Figures 11 and 12 which sohow the cooling rate/ distance relationships for both specimen thicknesses, it can be appreciated that there is a levelling off of the cooling rate/distance curve between 4.6, and 5.6 mm for the 3 mm thick specimens while for the 4 mm thick specimens no such levelling off takes place. Thus the quantitative metallography results correlate, in fine detail, with the cooling conditions in the specimens.

However it has been suggested (26) that the transformation product in welding can be related to the time the specimen spends in cooling from the A_1 temperature (or ~ 800"C) to 500"C. This time is claimed to be independent of the relative position of the region of interest with respect to the fusion zone and independent of the maximum temperature reached, depending only on the physico-chemical properties of the materials, the thermal in-put and the thickness of the material welded. Figure 63 shows the time spent in cooling from 825"C to 525"C for the 3 and 4 mm thick specimens as a function of distance from the centre of the fusion zone, which shows that the time on cooling from 825"C to 525"C is not strictly independent of distance but increases with distance from the centre of the fusion zone. This increase in cooling time with distance may not be very important industrially but obviously for a scientific interpretation of the microstructural results it must be taken into account.

Figure 64 shows the fraction of pearlite as a function of the maximum temperature reached. As can be seen no relationship independent of the thickness of the specimen exists. However, it is thought that for some industrial uses the relationship may be considered to give an estimate of the microstructure at a given point. This relationship has the disadvantage that it cannot be used in conjunction with continuous cooling data, and overall it is far better to employ the fraction transformed/cooling rate curves given in Figure 62.

5.6. Conclusions.

1. By a combination of quantitative metallography and a measurement of the thermal history of the specimens as a function of distance from the centre of the fusion zone, the PST weld simulator is capable of giving semi –quantitative in– formation on the transformations taking place in the weld HAZ in a Fe-O.6C alloy.

2. The transformation of the ferrite present in the original microstructure is observed to initiate at its boundary with the pearlite and to finish under a heating rate of 50"C s ^{1} at 780"C.

3. The pearlite is observed to transform rapidly in the eutectoid temperature region, this reaction initiating at "faults" in the microstructure.

4. The pearlite to austenite reaction is observed to start at these "faults" and proceed to form an enclave of non-homogeneous austenite in the pearlite colony. Dissolution of the cementite lamellæ from both the tips and sides has been detected.

5. This non-homogeneous austenitic region decomposes on cooling into "martensite" and nodules of pearlite with a fine interlamellar spacing.

6. In regions near to the fusion zone the original pearlite structure is completly transformed to an austenite which is, to a greater or lesser extent, homogeneous. This region, on cooling, transforms to form martensite and nodules of pearlite of a fine interlamellar spacing, the proportion of pearlite decreasing in regions closer to the fusion zone.

7. Inflection points in the cooling curves obtained in the PST weld simulator were detected. These inflections were found not to represent necessarily the temperature of a transformation taking place at that point in the specimen but were due to the fact that the cooling rate at each point in the specimen is influenced by the recalescence effect of the pearlite transformation, not only at the point of transformation but also in regions adjacent to it. Thus, the temperatures found reflect the overall limits of temperature in the specimen during which, in some part of the specimen, the pearlite transformation is taking place.

8. By comparingthe CCT data determined for this steel with the cooling curves measured in the PST weld simulator, the temperature at which each point in the specimen "ought to" transform if it were only under continuous cooling conditions was determined and found to be within the temperature intervals of the inflection points registered in the cooling curves determined from the PST weld simulator.

9. From a detailed analysis of the results, it is postulated that in regions close to the fusion zone where the austenite is homogeneous, its behaviour in the PST weld simulator is similar to that under continuous cooling conditions whereas in regions nearer to the non-affected zone, where the austenite is not complety homogeneous, it transforms to pearlite at a slightly higher temperature than that predicted from continuous cooling data. Inhomogeneities in the austenite thus promote the nucleation of pearlite.

10. The cooling rate from 625"C to 525"C and in particular from 525"C to 425"C is found to determine the fraction of pearlite formed independent of specimen size, and are the most critical temperature regions for the development of a pearlite nucleus. At cooling rates of above 53"C s ^{1} in the 625 — 525"C temperature interval pearlite is not found.

11. The time spent in cooling from 825"C to 525"C and the maximum temperature reached are found not to be as accurate a variable to define the fraction of pearlite formed as is the cooling rate between the limits previously stated.

5.7. Recomendations.

In view of the success of the PST weld simulator in providing a semiquantitative description of the transformations occurring during simulated welding of a Fe-O.6 C steel, it is thought that this technique should be extended to study more complicated alloys, for example superalloys. A study of a superalloy was envisaged in this contract, but specimens were not provided by the European Office of Aerospace Research and Development as offered in Section F-1, A of the contract and requested in the Semi − Annual Progress Report.

At the same time the results obtained in the metallographic study by SEM, recommend that this work should be continued systematically. New reagents and etch conditions would help to establish a more precise interpretation of the solidstate reactions taking place and products formed as a consequence of the non-conventional heat treatment in a HAZ. As transformations in progress can be frozen-in, mechanisms for these transformations might be established.

6. Literature Cited

1. D.F. ADAMS and A.J. MOMBRUM, Metallurgia, Oct. 1969, 80, (480), 131-134.

2. E. SMITH, M.P. COWARD, J.L. BROWN and R.L. APPS, Welding, Dec. 1970, 38 (12), 496-504.

3. P.W. HOLSBERG and W.G. SCHREITZ, Methods of High-Alloy Weldability Evaluation, 1970, 22-27.

4. P.F. MARTIN and C. ROQUES, Methodos of High-Alloy Weldability Evaluation, 1970, 45-51.

5. J.M. LOWES, K.D. RICHARDSON and D.M. HADDRILL, Metal Construction, Oct. 1972, 4, (10), 373-375.

6. D. LEVERT, M. HUBERT and C. MESSAGER, Rev. Mét., Nov. 1972, 69, (11), 767-779.

7. R.H. PHILLIPS and M.F. JORDAN, Welding Research Internat. 1973, 3, 59-68.

8. A. VINCKIER, Welding Research Related to Power Plant, Southampton, 1972, 1975, 336-355.

9. L.E. GUKASYAN, Welding Production, Nov. 1976 (11), 50-51.

10. L.V. IVANOV, E.P. MOTUS, and Yu. A. TSYGANOV. Welding Production, Feb. 1977 (2), 53-55.

11. J. MYERS, Met. Technol. Aug. 1977, 4, (8), 411-412.

12. A.P. DROZVOV, I.M. SHVETS, L. V. DEVOV, V.V. NECHAEV and V.N. FOMENKO. Ind. Lab. 1977, 43 (6), 831-833.

13. E. SCHMIDTMANN and W. DIETER THINNES, Stahl Eisen, 1 Dec. 1977, 97, (24), 1197-1201.

14. A.G. GRIGOR'YANTS and V.A. VINOKUROV, Automatic Welding, Oct. 1977, (10), 8-11.

15. L. CALLEGARI and T. VENTURRELLI, Boll Tec. Finsider, Oct. 1977 (368), 621-628.

16. S.I. ERMAKOV, V.A. VINOKUROV and A.G. GRIGOR'YANTS, Welding Production, Feb. 1978, (2), 56-57.

17. P. BERNASOVSKY, M. INAGAKI AND T. KASUAGAL, ZVARANIE. Jan. 1978, 27, (1), 13-16.

18. R. RCHOFIELD and R.T. WEINER, Metal Construction, Feb. 1974, 6 (2), 45-47.

19. R. SCHOFIELD and R.T. WEINER, Metal Construction, Feb. 1974, 6 (2), 45-47.

20. F.A. CALVO, K.P. BENTLEY and R.G. BAKER. BWRA, Abington, 1963, 71pp.

21. F.A. CALVO, A. REVUELTA and L. MONPEAN. "Research report of the U.S. Department of the Army, European Research Office, Contract numbers DA 91 591 EUC 1485 and DA 91 591 EUC 1771, 1960-1962.

22. F.A. CALVO, Progress reports, Fundación Juan March, 1962-1964.

23. A.R. MARDER and B.L. BRAMFITT, Metall. Trans. A. Nov. 1975, 6A, (11), 2009-2014.

24. A.R. MARDER and B.L. BRAMFITT, Metal. Trans. A, June 1976, 7A, (6), 902-905.

25. E.A. LORIA, Metallurgia, Nov. 1969, 80, (481), 175-178.

26. F. LOPEZ GRACIANI, Revista de Soldadura, July-September, 1976, Volume VI, (3), 105-122.

27. D.R.H. JONES and G.J. MAY, Acta Met., Jan 1975, 23, (1), 29-34.

28. D.R.H. JONES, Metal Sci., Feb. 1974, 8, 37-40.

29. D.R.H. JONES, Mater Sci. Eng., Aug-Sept. 1974, 15, (2/3), 203-209.

30. B.G. MELLOR. Ph.D. Thesis, Cambridge University, 1973.

31. B.G. MELLOR and D.V. EDMONDS, Met. Trans. A, 8A, 1977, 763-771.

32. L.D. GRAHAM and R.W. KRAFT, Trans. AIME, 1966, 236, 94.

33. B.G. MELLOR, D.V. EDMONDS, and G.A. CHADWICK, Metal Science Journal 1978, 11. 439-444.

34. R.F. MEHL and W.C. HAGEL, Progress in Metal Physics, 1954, (6), 74-134, Pergamon Press, New York and London.

35. F.C. HULL and R.F. MEHL, 1942, Trans. Amer. Soc. Metals, 30, 381.

36. F.C. HULL, R.A. COLTON and R.F. MEHL, Trans. Amer Inst. Min. (Metall) Engrs 1942, 150, 185.

7. Tables and Figures.

TABLE I

Ferrite to Austenite transformation.

Specimen thickness	α → γ limits Distances from centre of fusion zone, Figs. 48-51	α → γ Temperature limits Figs. 13-14	Heating rate from 725 to 825°C at distances of α → γ transformation Figs. 9-10	Time above 725°C corresponding to the high temperature border of the α → γ region Figs. 15-16	Thermal gradient at distances of α → γ transformation Figs. 5-6
mm	mm	°C	°C s⁻¹	s	°C mm⁻¹
3	6.8 to 7.4	775 to 710-710	50	2.5	120
4	5.25 to 6.05	780 to 715-710	50	2.5	120

TABLE II

The Austenite to "pearlite" transformation.

Specimen thickness	γ → pearlite limits. Dist. from centre of fusion zone Figs. 50-53	50% pearlite Dist. from centre of fusion zone Figs. 50-53	Time of γ above 725°C for γ → pearlite limits Figs. 15-16	Time of γ above 725°C for 50% pearlite position Figs. 15-16	Max temps. reached in γ at distances of γ → pearlite reaction Figs. 13-14	Max temp. corresponding to 50% pearlite position Figs. 13-14	Thermal gradient at distances of γ → pearlite reaction Figs. 7-8
mm	mm	mm	s	s	°C	°C	°C mm⁻¹
3	4.25 to 6.5	6.2	9.5 to 4	4.8	1150 to 810	850	55
4	3.15 to 5.0	4.45	7.5 to 3.8	5.3	1150 to 810	885	55

TABLE II (Continued)

Specimen thickness	Cooling rates 725 - 625°C at distances of γ → pearlite reaction Figs. 11-12	Cooling rates 625 - 525°C at distance of γ → pearlite reaction Figs. 11-12	Cooling rates 725° - 525°C at distance of γ → pearlite reaction Figs. 11-12	Cooling rates 725°C - 425°C at distances of γ → pearlite reaction Figs. 11-12
mm	°C s⁻¹	°C s	°C s	°C s⁻¹
3	85 to 67	58 to 48	71.5 to 57.5	61.3 to 49.6
4	100 to 70	65 to 47	76.0 to 58.5	64.0 to 50.6
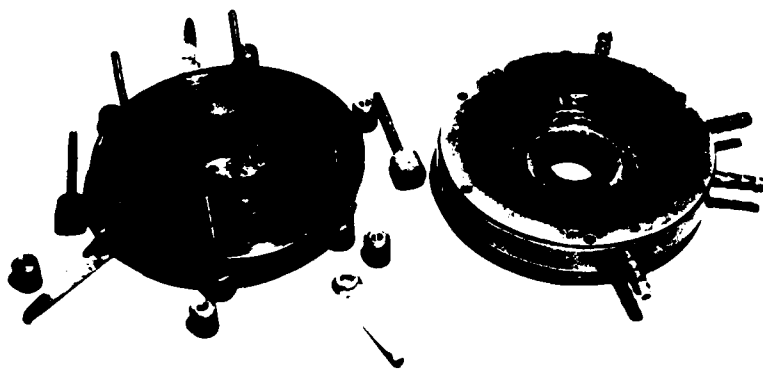
Figura 1. Welding Chamber.
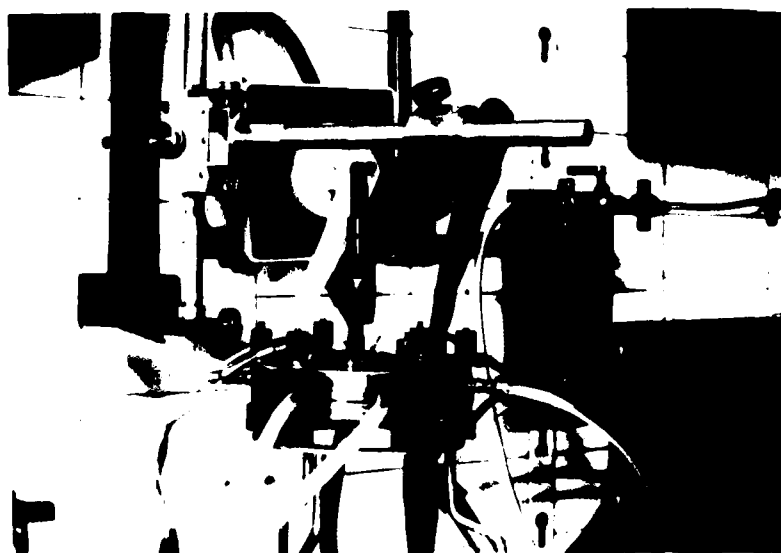
Figure 2. PST weld simulator.
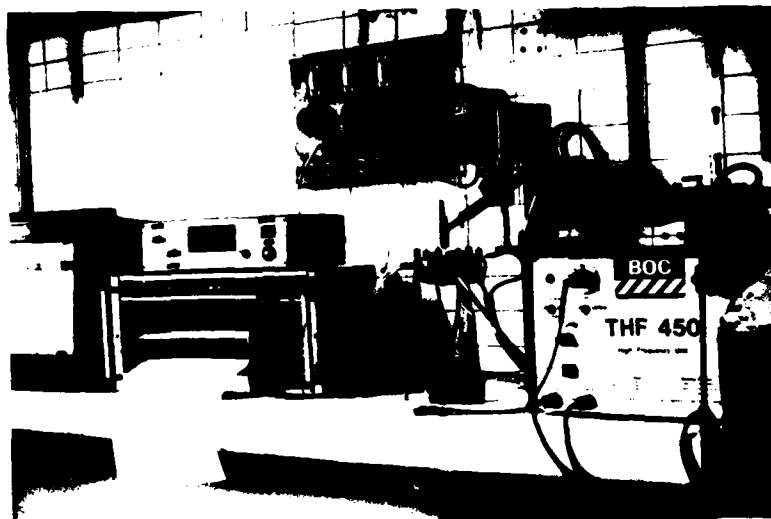
Figure 3. Overal, view of the PST weld simulator.
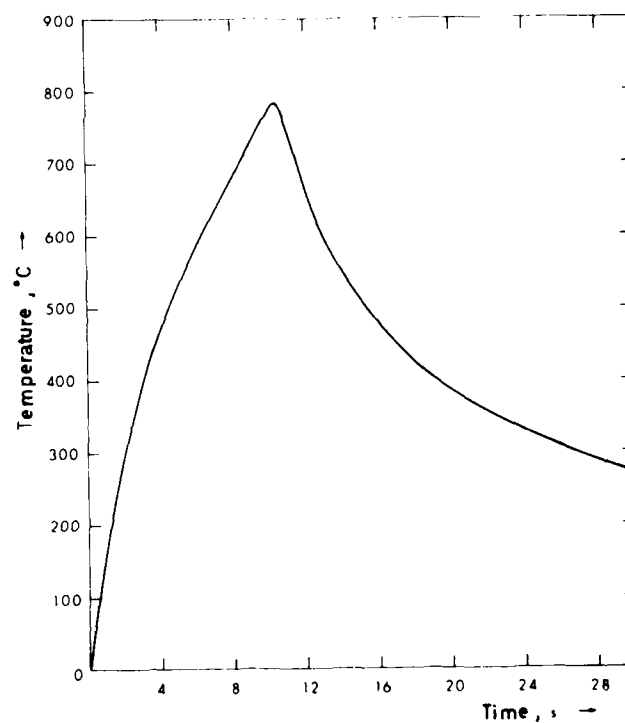
Figure 4. Temperature as a function of time during the welding cycle. This curve corresponds to a thermocouple spot welded at 5.20 mm from the centre of the fusion zone in a 4 mm thick specimen.

33
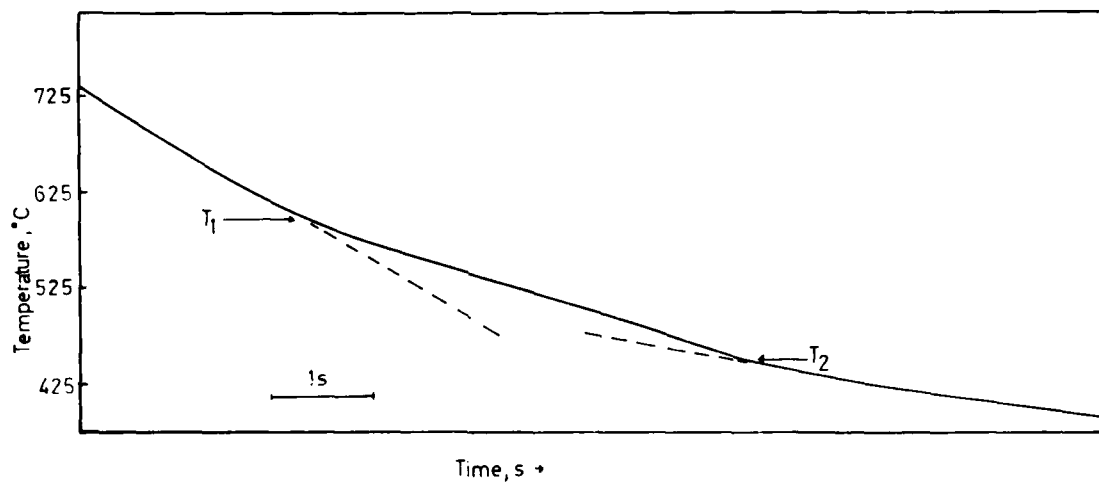
Figure 4b. Part of Figure 4 on a larger scale shwing the inflection points T_1 and T_2 detected in the cooling curve.
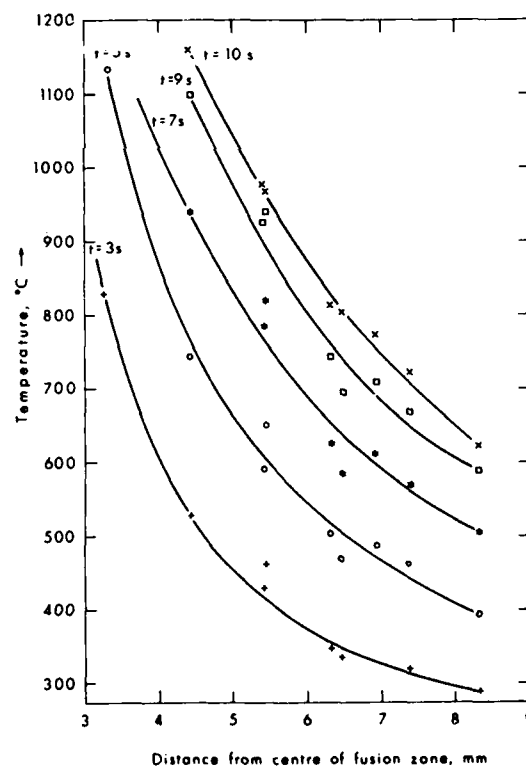
Figure 5. The temperature reached at different times during the heating cycle (t — 3, 5, 7, 9, 10 s) as a function of distance from the centre of the fusion zone for specimens 3 mm thick.
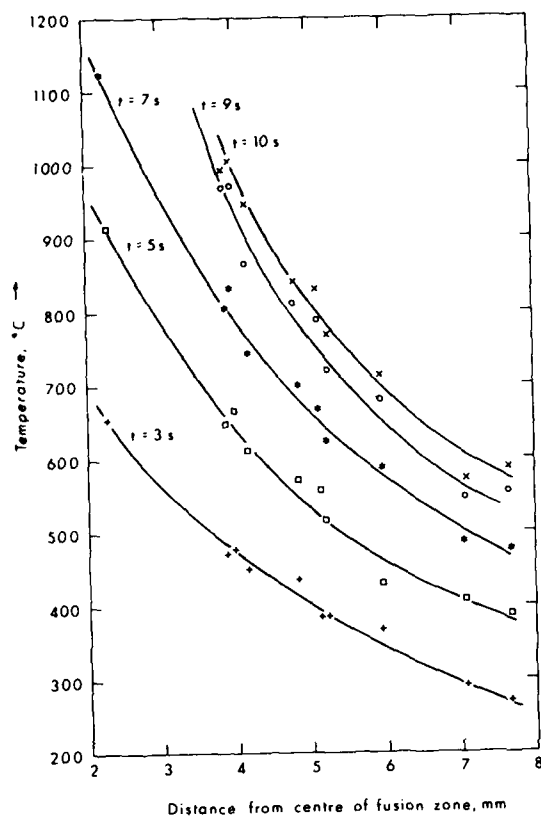
Figure 6. The temperature reached at different times during the heating cycle (t = 3, 5, 7, 9, 10 s) as a function of distance from the centre of the fusion zone for specimens 4 mm thick.
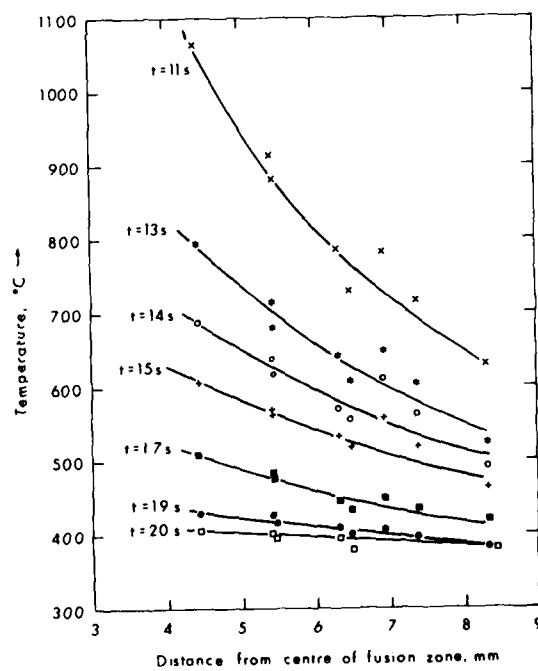
Figure 7. The temperature reached at different times during the cooling cycle (t = 11, 13, 15, 17, 19 s) as a function of distance from the centre of the fusion zone for specimens 3 mm thick.
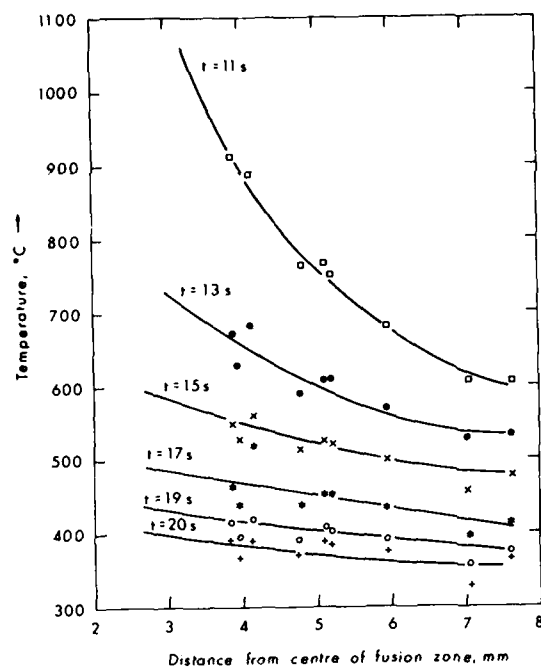
Figure 8. The temperature reached at different times during the cooling cycle (t = 11, 13, 15, 17, 19 s) as a function of distance from the centre of the fusion zone for specimens 4 mm thick.
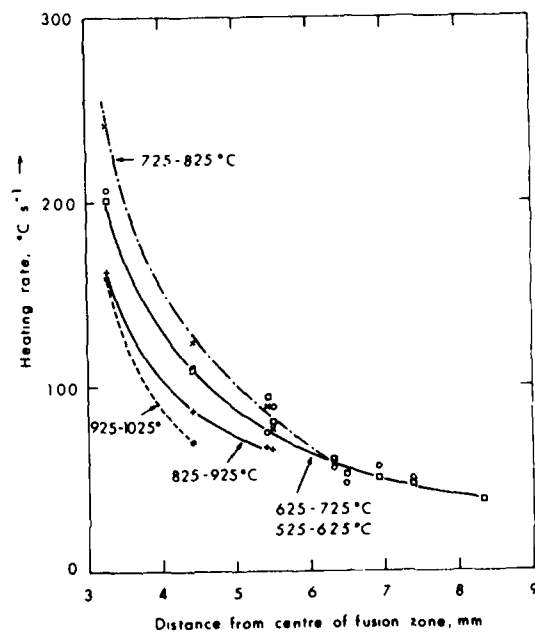
Figure 9. The heating rate within various temperature intervals as a function of distance from the centre of the fusion zone for specimens 3 mm thick.

36
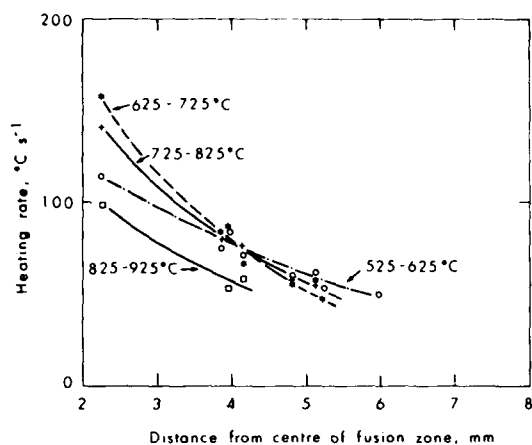
Figure 10. The heating rate within various temperature intervals as a function of distance from the centre of the fusion zone for specimens 4 mm thick.
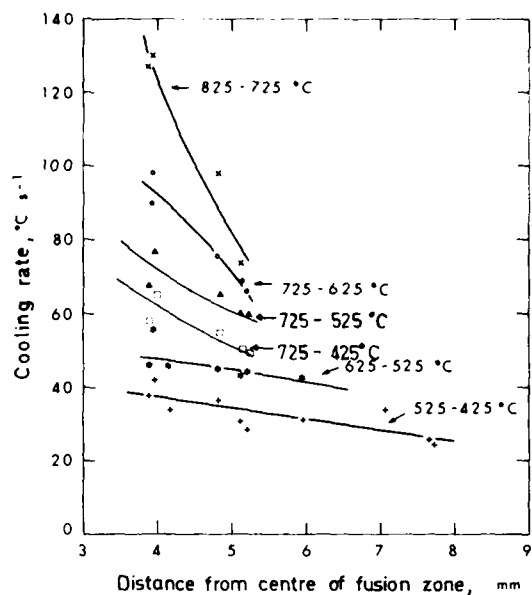
Figure 12. The cooling rate within various temperature intervals as a function of distance from the centre of the fusion zone for specimens 4 mm thick.
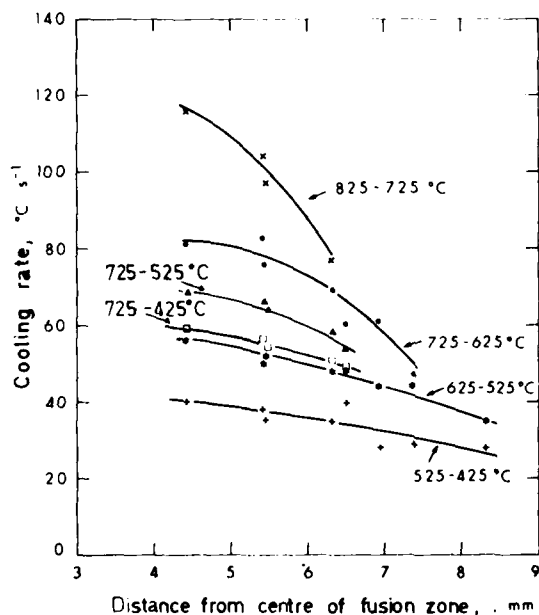
Figure 11. The cooling rate within various temperature intervals as a function of distance from the centre of the fusion zone for specimens 3 mm thick.
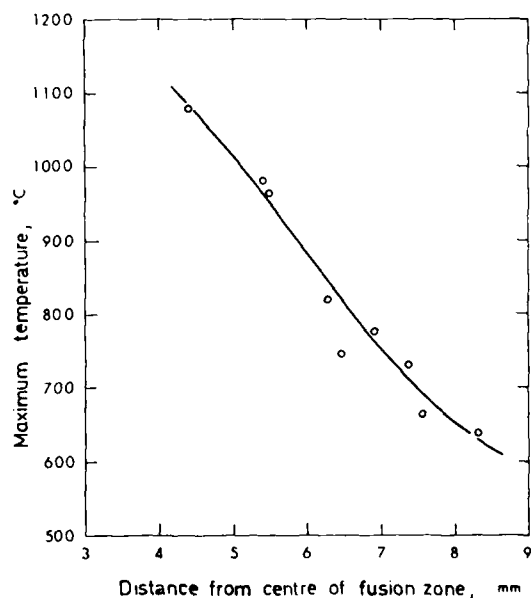
Figure 13. Maximum temperature reached as a function of distance from the centre of the fusion zone for specimens 3 mm thick.

37
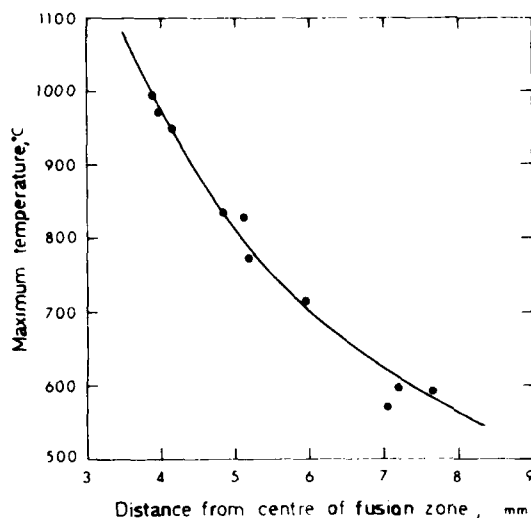
Figure 14. The maximum temperature reached a function of distance from the centre of the fusion zone for specimens 4 mm thick.
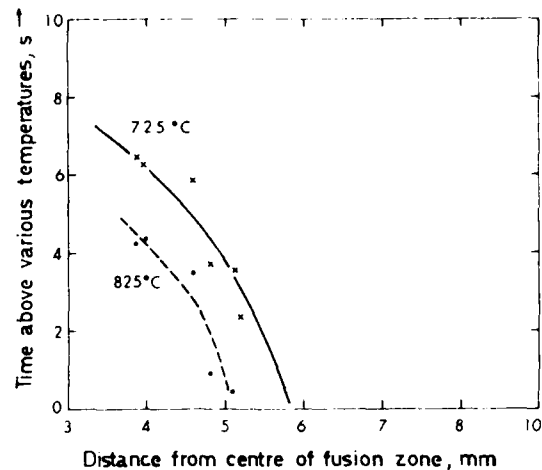
Figure 16. The time above 725"C and above 825"C as a function of distance from the centre of the fusion zone for specimens 4 mm thick.
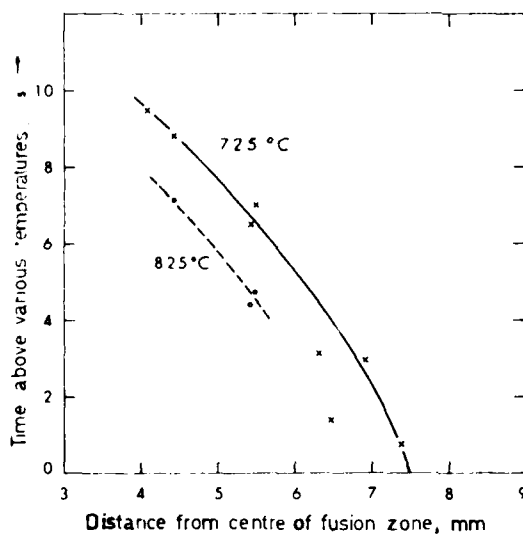
Figure 15. The time above 725"C and above 825"C as a function of distance from the centre of the fusion zone for specimens 3 mm thick.
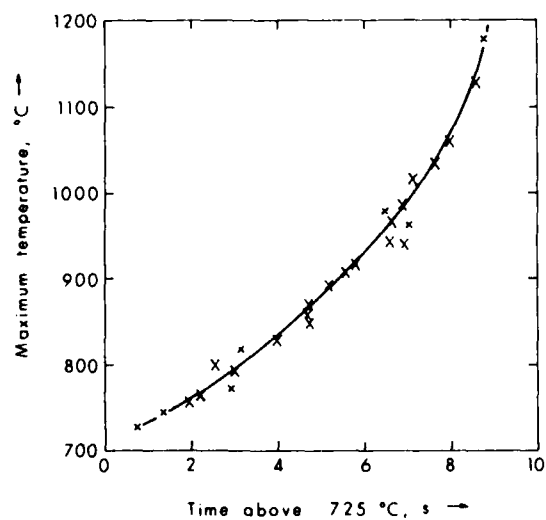
Figure 17. The maximum temperature reached as a function of time above 725"C for specimens 3 mm thick.
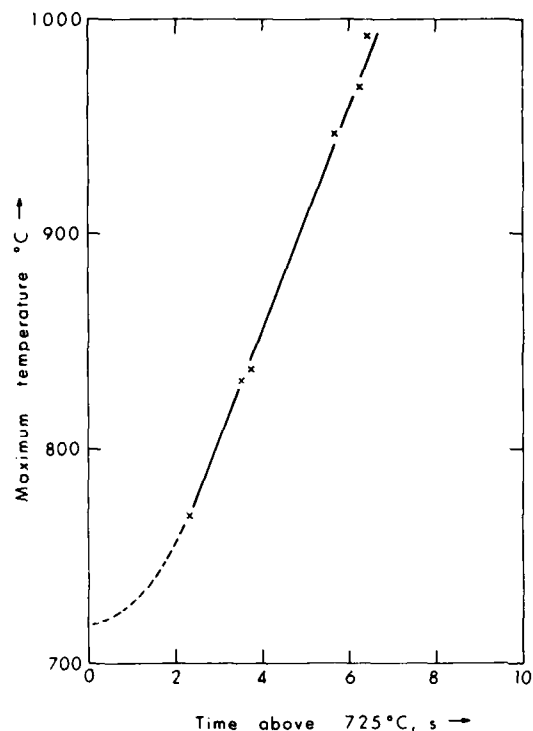
Figure 18. The maximum temperature reached as a function of time above 725"C for specimens 4 mm thick.
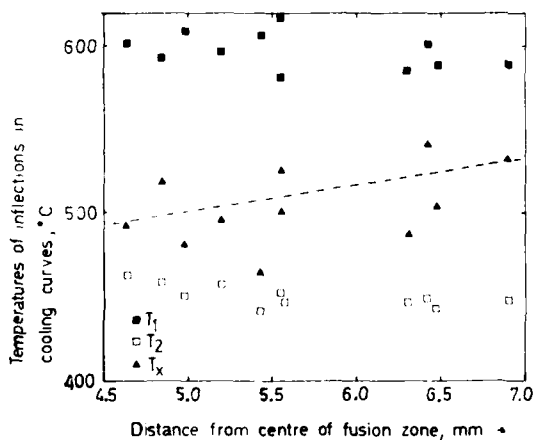
Figure 19. The temperature corresponding to the inflections detected in the weld simulation cooling curves (T_1 and T_2) as a function of distance from the centre of the fusion zone for a 3 mm thick specimen. The temperature at which the regions of the specimen "ought to" transform (T_x) if they conform to continuous cooling data are also marked.
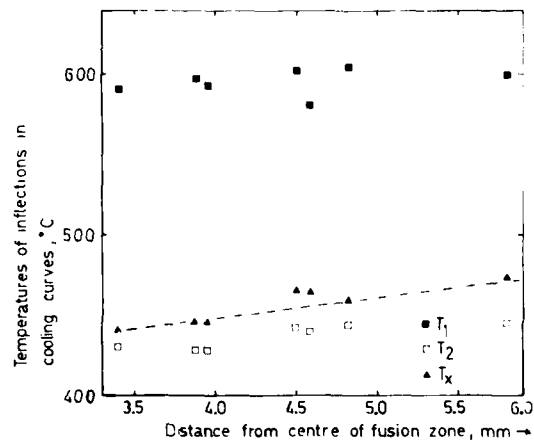
Figure 20. The temperature corresponding to the inflections detected in the weld simulation cooling curves (T_1 and T_2) as a function of distance from the centre of the fusion zone for a 4 mm thick specimen. The temperature at which the regions of the specimen "ought to" transform (T_x) if they conform to continuous cooling data are also marked.

39
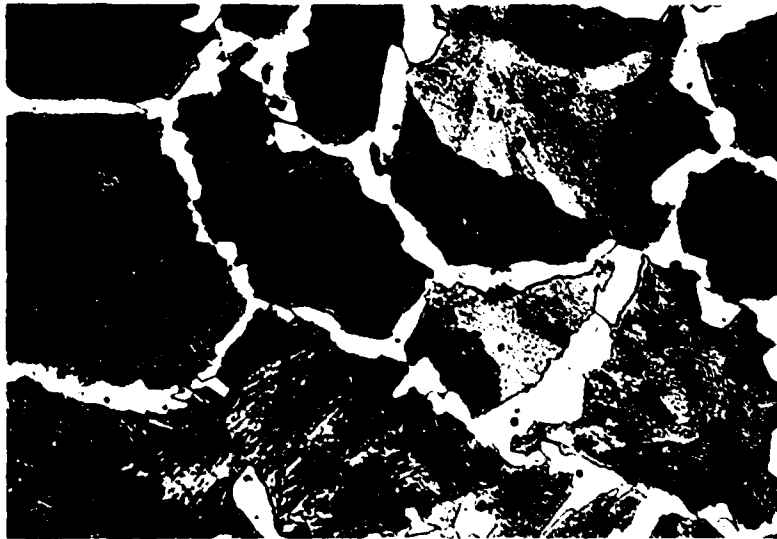
Figure 21. Microstructure of specimen prior to weld simulation x325.

Figure 22. Microstructure of specimen prior to weld simulation x800.

40
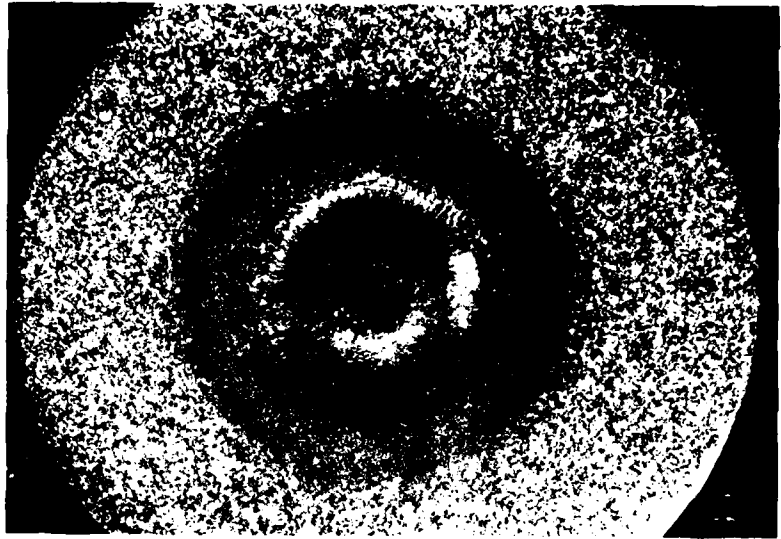
Figure 23. Macrograph of specimen after weld simulation x4.5.
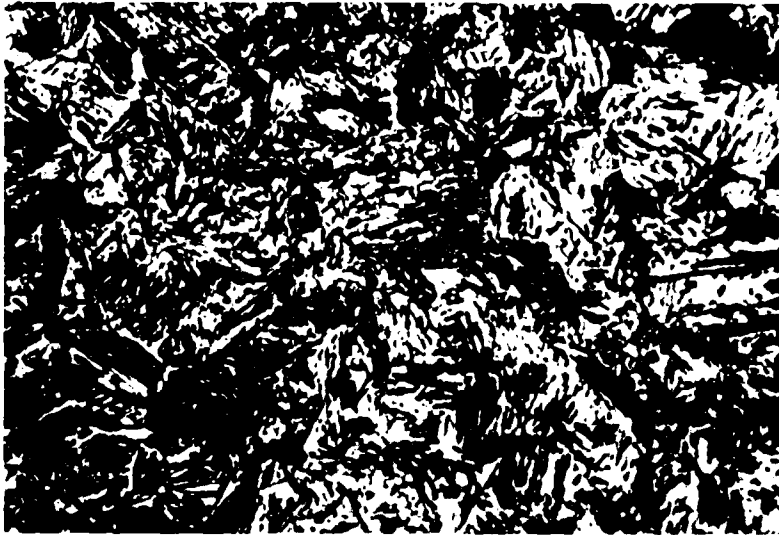
Figure 24. Microstructure of a region close to the fusion zone x800.

41
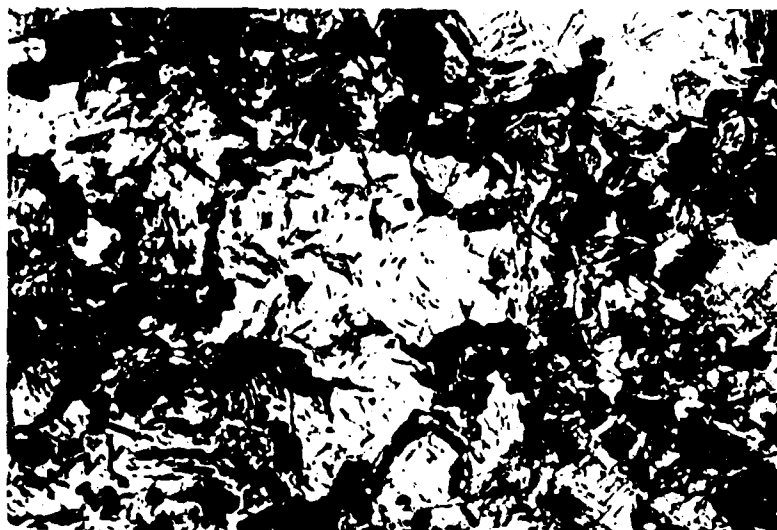
Figure 25. Microstructure of a region further away from the fusion zone than Figure 24 x800.
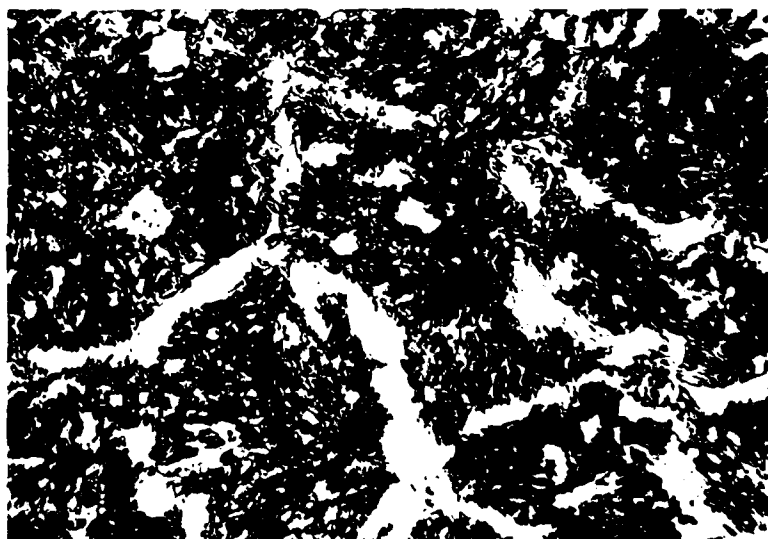
Figure 26. Microstructure of the HAZ near the border with the non-affected zone x325.
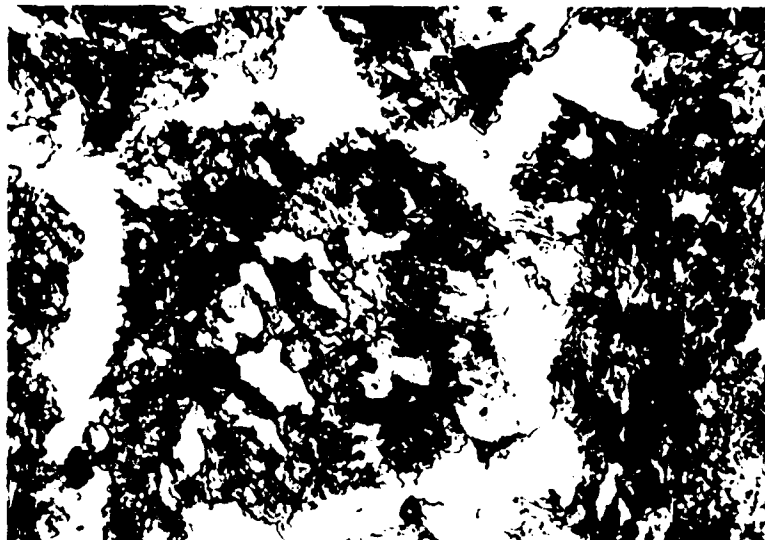
Figure 27. Microstructure of the HAZ near the border
with the non-affected zone x800.
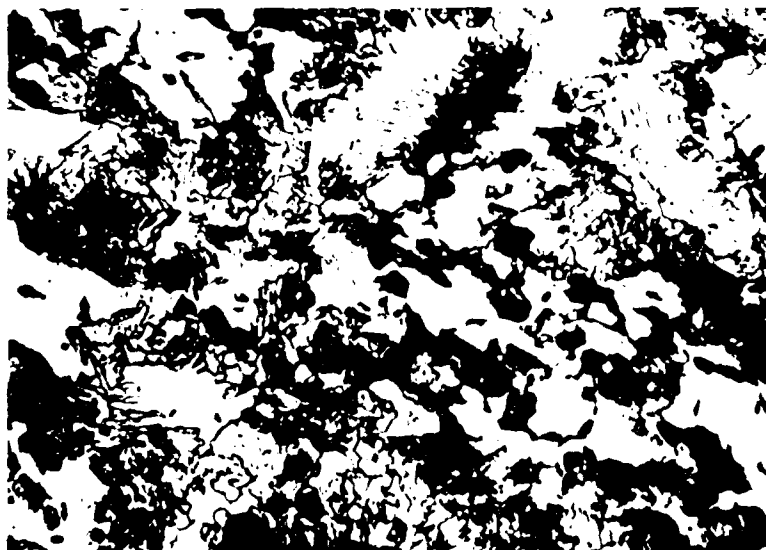
Figure 28. Microstructure of the HAZ further towards
hte fusion zone than Figures 26 and 27 x800.

43

Figure 29. SEM of the microstructure of the non-affected zone x2200.

Figure 30. SEM of the microstructure close to the fusion zone × 2200

Figure 31 SEM of the microstructure closer to the non affected zone than Figure 30. x2200.

Figure 32. SEM of the microstructure closer to the non affected zone than Figure 31. x2200.

45

Figure 33. SEM of the microstructure closer to the heat affected zone than Figure 32. ×2700.

Figure 34. A region of figure 33 at higher magnification ×6600

46
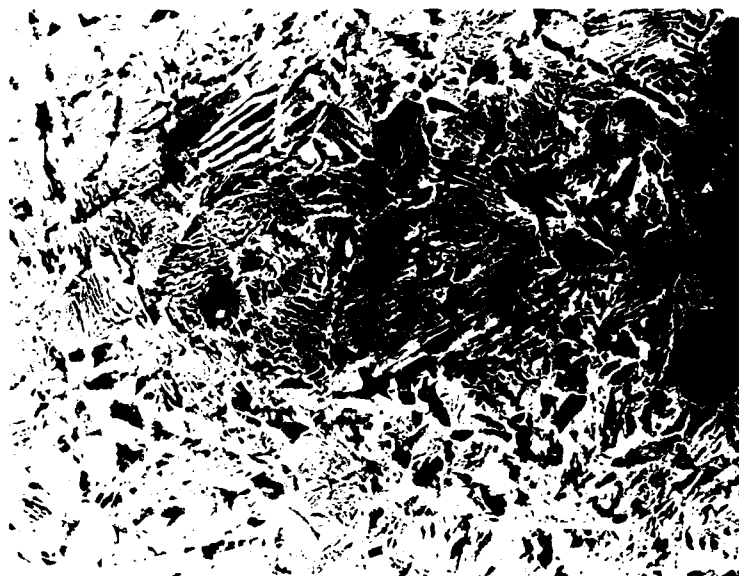
Figure 35 SEM of the microstructure closer to the non-affected zone than Figure 33 x2200.

Figure 36 SEM of the microstructure closer to the non-affected zone than Figure 33 x2200

47

Figure 37. SEM of the microstructure at the boundary
of the HAZ with the non-affected zone x2200.

Figure 38. SEM of the microstructure at the boundary of
the HAZ with the non-affected zone x9400.

48
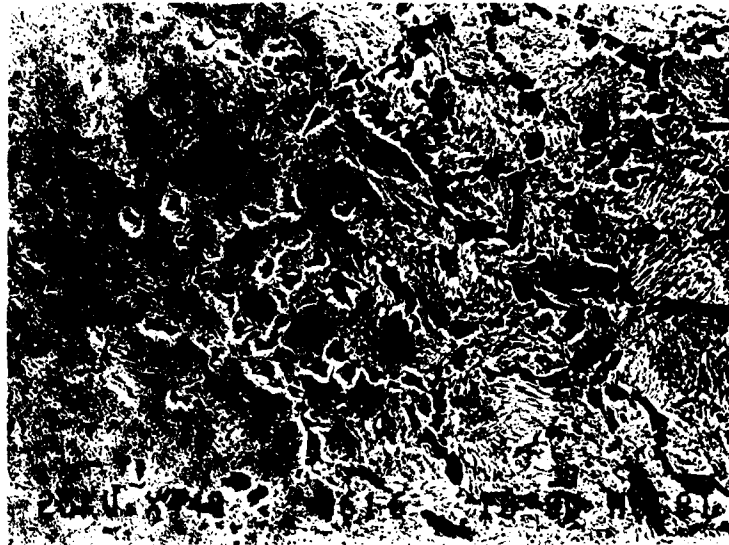
Figure 39. SEM of the microstructure at the boundary of the HAZ with the non-affected zone x440.

Figure 40. SEM of the microstructure in a region where the ferrite to austenite transformation is nearing completion x600.

49

Figure 41. SEM of the microstructure at the boundary of
the HAZ with the non-affected zone. x4000.

Figure 42. SEM of the microstructure in the HAZ near the
boundary with the non-affected zone. x11 000.
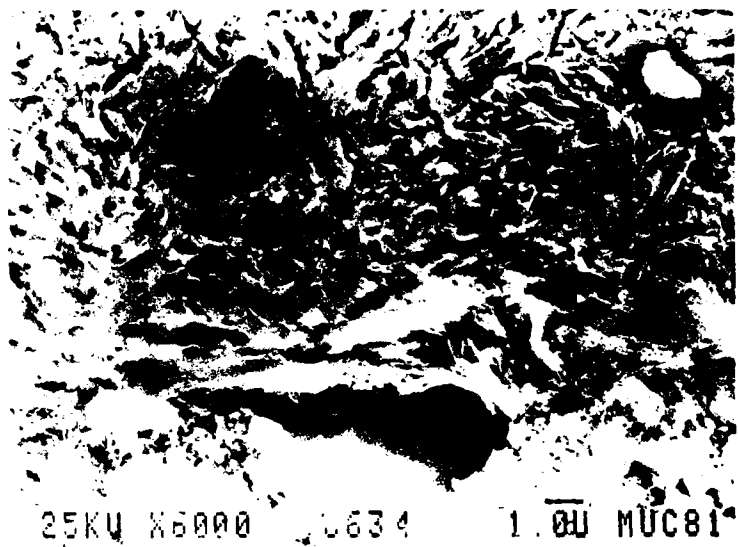
Figure 43. SEM of the microstructure in a region of Figure 40 x6000.

Figure 44. SEM of the microstructure in a region slightly nearer to the fusion zone than Figure 43 x2600
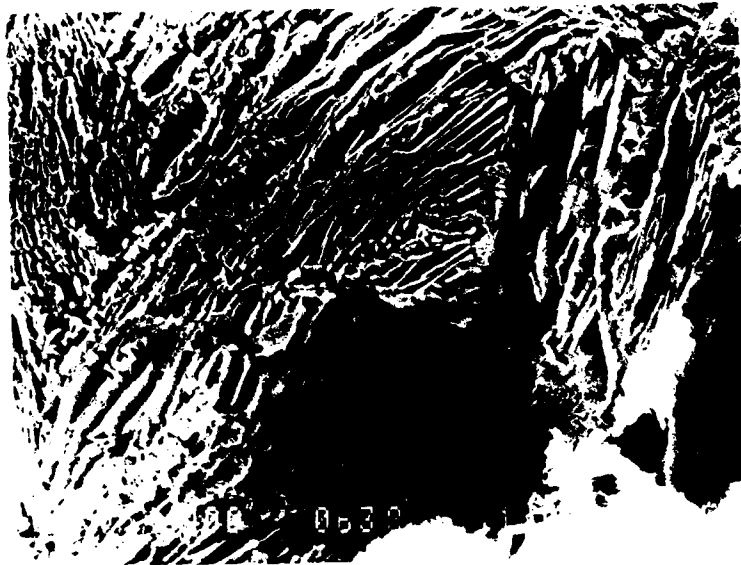
Figure 45. SEM of the microstructure at the boundary of the HAZ with the non-affected zone. Etched with picral x4400.

Figure 46 SEM of the microstructure in a region in the HAZ close to the boundary with the non-affected zone. Etched with picral x6600.

Figure 47. SEM of the microstructure in a region in the HAZ close to the boundary with the non-affected zone. Etched with picral x7800.

Distance from centre of fusion zone, mm
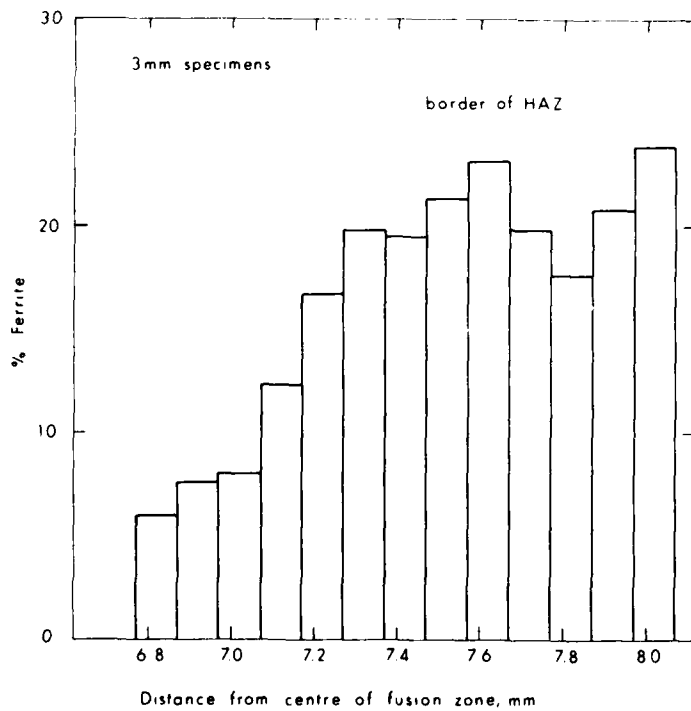
Figure 48. Histogram showing the percentage of ferrite in the microstructure as a function of distance from the centre of the fusion zone for specimens 3 mm thick.
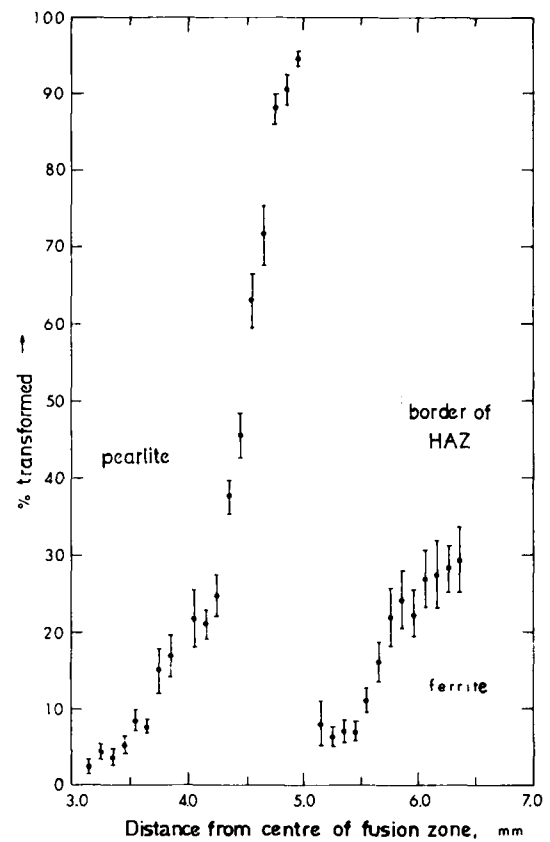
53
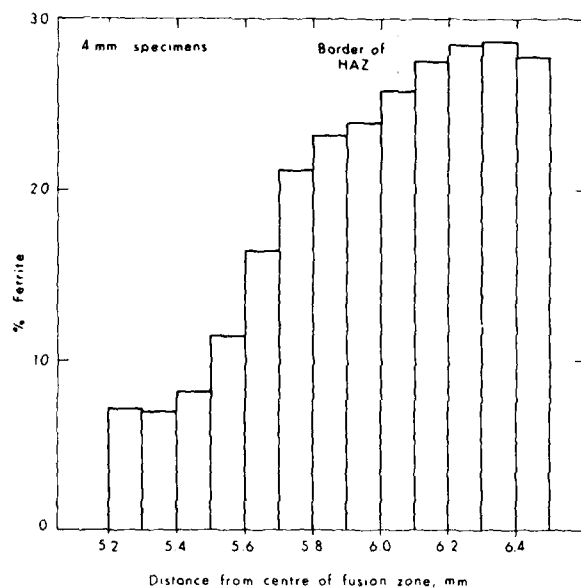
Figure 49. Histograms showing the percentage of ferrite in the microstructure as a function of distance from the centre of the fusion zone for specimens 4 mm thick.
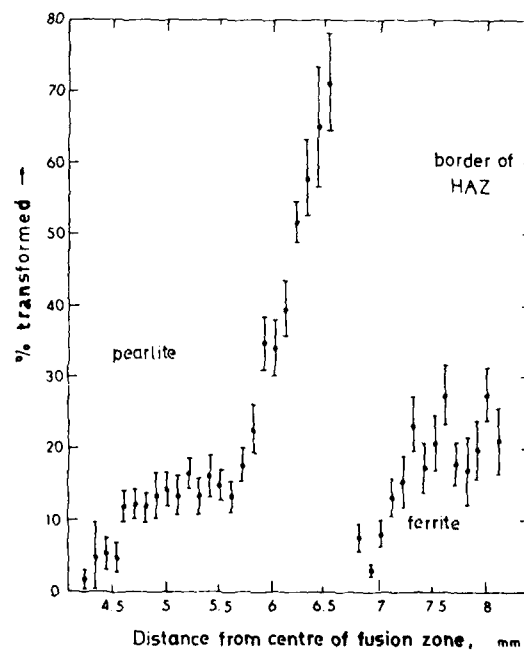
Figure 50. The percentage of ferrite and "pearlite" in the microstructure as a function of distance from the centre of the fusion zone for specimens 3 mm thick.
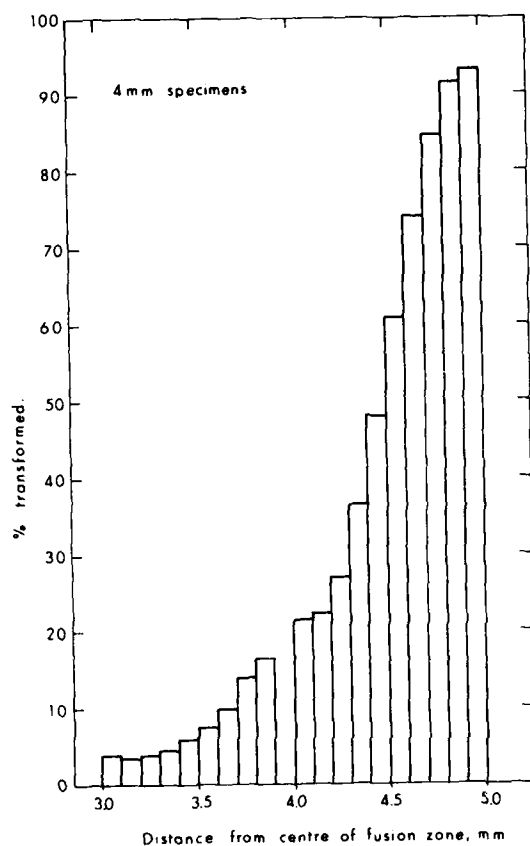
54

Figure 51. The percentage of ferrite and "pearlite" in the microstructure as a function of distance from the centre of the fusion zone for specimens 4 mm thick.

Figure 52. Histogram showing the percentage of 'pearlite' in the microstructure as a function of distance from the cente of the fusion zone for specimens 3 mm thick.

55

Figure 53. Histogram showing the percentage of 'pearlite' in the microstructure as a function of distance from the centre of the fusion zone for specimens 4 mm thick.
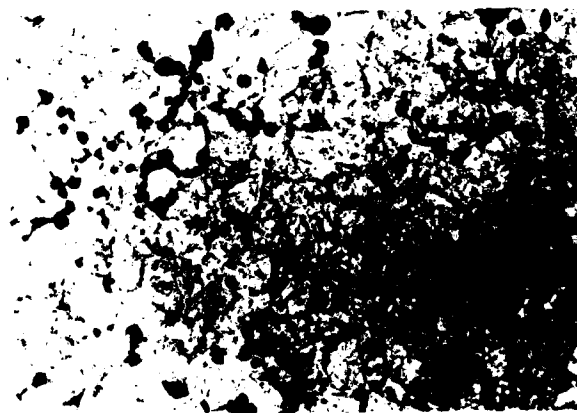
Figure 54. Fe-O.6C alloy partially transformed by continuous cooling at 53°C s⁻¹ in the 625° to 525°C interval x230.
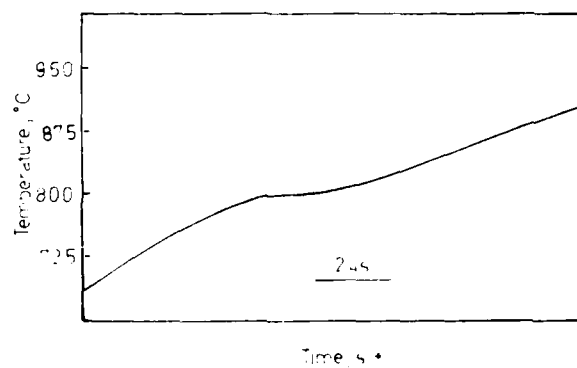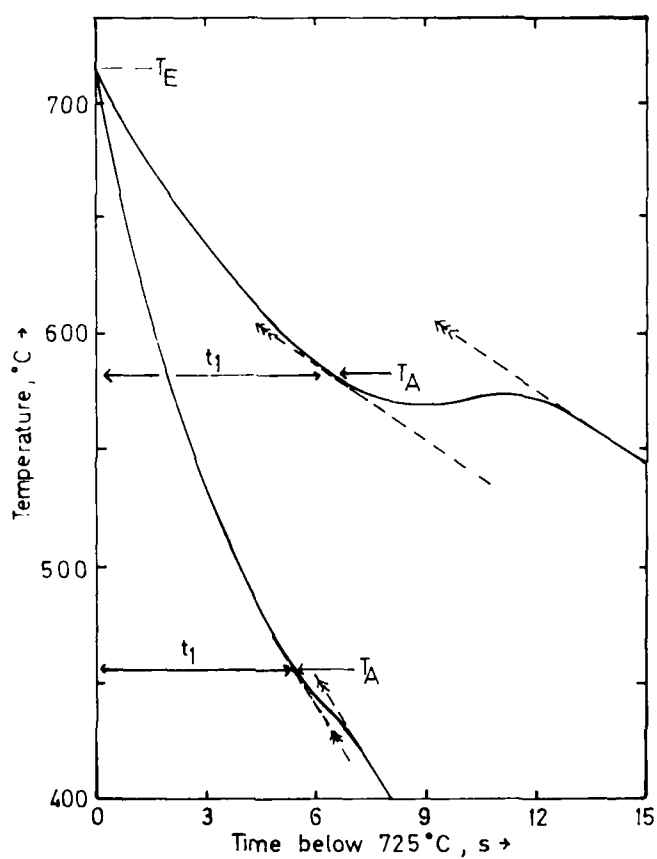
56

Figure 55. Continuous heating curve.

Figure 56. Continuous cooling curves at a low and high
cooling rate and the construction used to
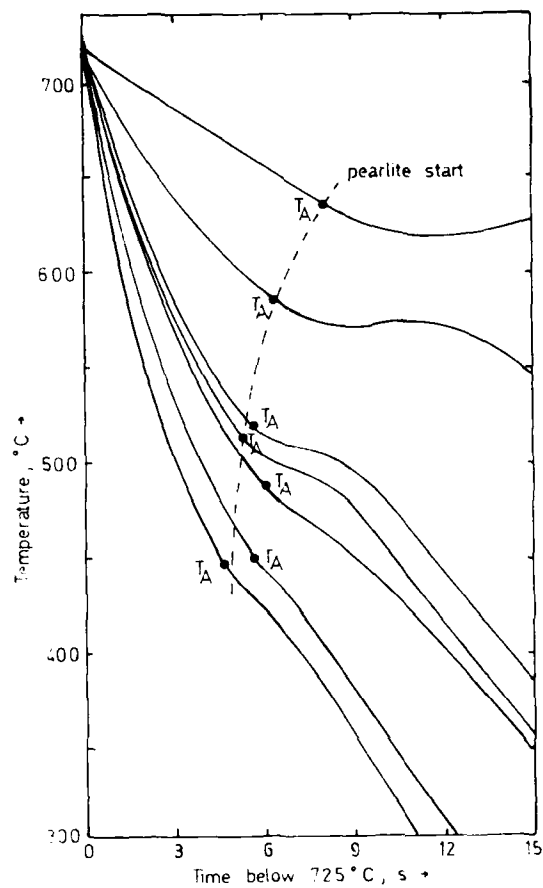define the T_A temperature, and t_1 time.

Figure 57. Various continuous cooling curves defining the start of the pearlite reaction as a function of temperature and time below 725°C.
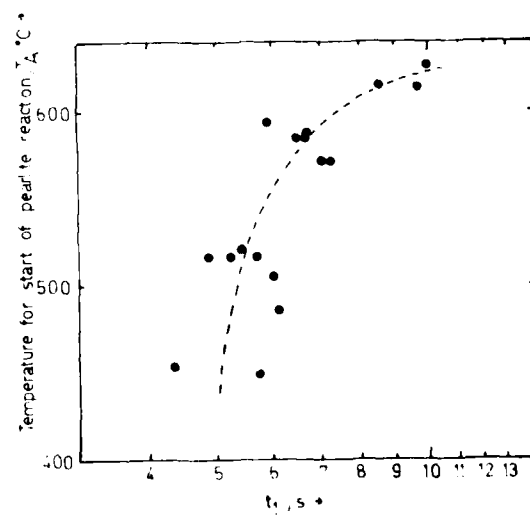

Figure 58. Temperature for the start of the pearlite reaction, T_A, under continuous cooling conditions as a function of time, t_1, below 725°C.

Figure 59. The temperature for the start of the pearlite reaction, T_x, under continuous cooling conditions as a function of cooling rate in various temperature intervals.
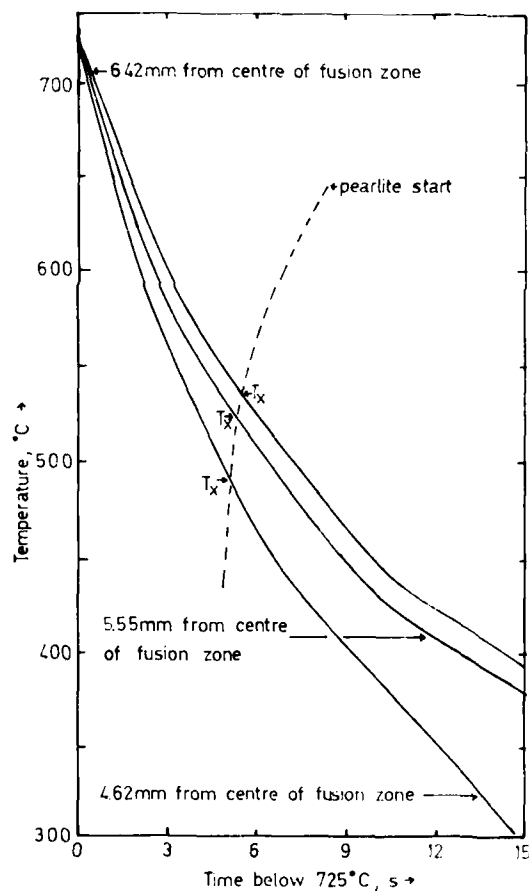

Figure 60. Cooling curves observed in the PST weld simulator for 3 mm specimens superimposed on the curve for the start of the pearlite reaction under continuous cooling conditions (Figure 57).
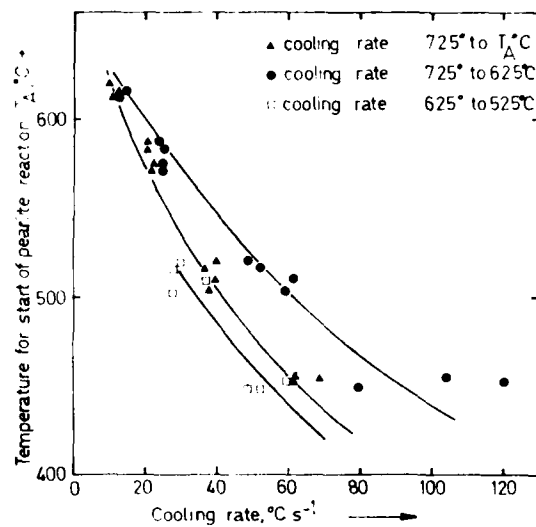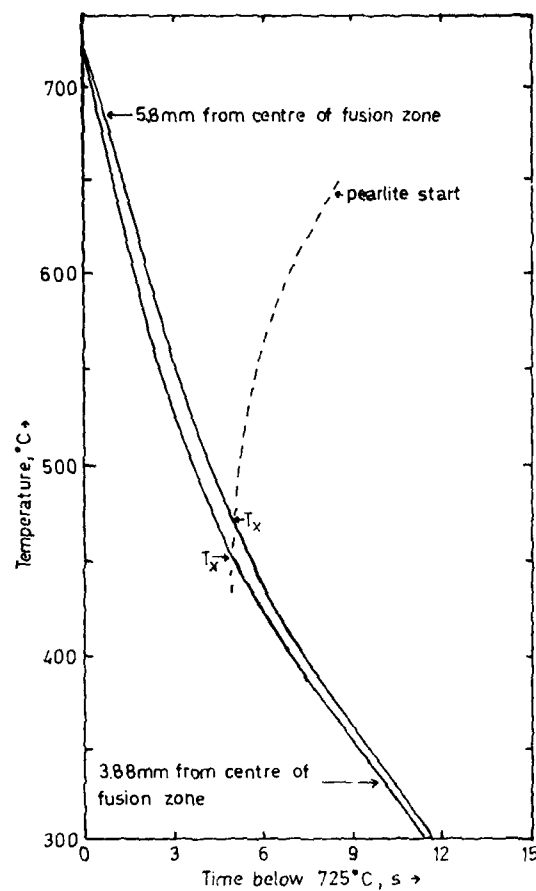
59

Figure 61. Cooling curves observed in the PST weld simulator for 4 mm specimens superimposed on the curve for the start of the pearlite reaction under continuous cooling conditions (Figure 57).
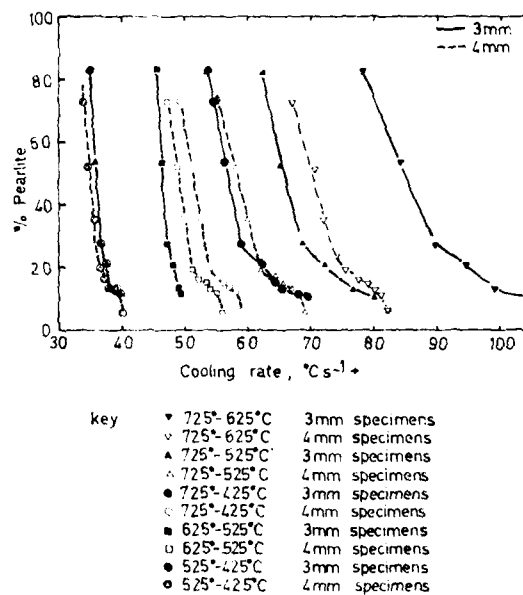

key			
▼	725°-625°C	3mm	specimens
▽	725°-625°C	4mm	specimens
▲	725°-525°C	3mm	specimens
△	725°-525°C	4mm	specimens
●	725°-425°C	3mm	specimens
○	725°-425°C	4mm	specimens
■	625°-525°C	3mm	specimens
□	625°-525°C	4mm	specimens
●	525°-425°C	3mm	specimens
○	525°-425°C	4mm	specimens

Figure 62. The percentage of pearlite formed in the PST weld simulator as a function of cooling rate within various temperature intervals for 3 and 4 mm thick specimens.
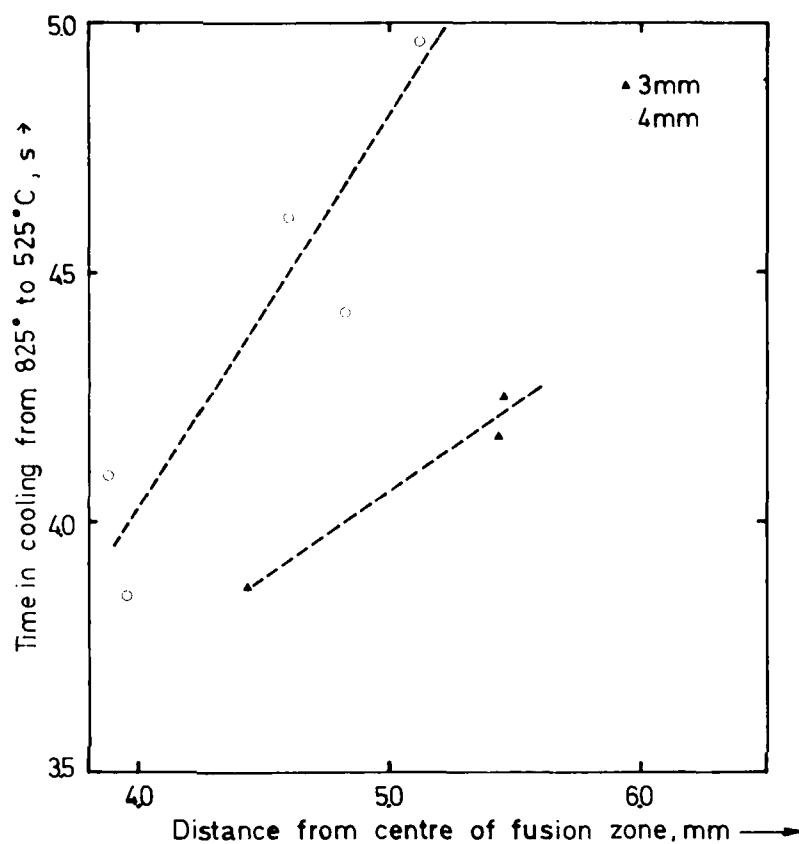
Figure 63. The time in cooling from 825°C to 525°C
as a function of distance from the centre of
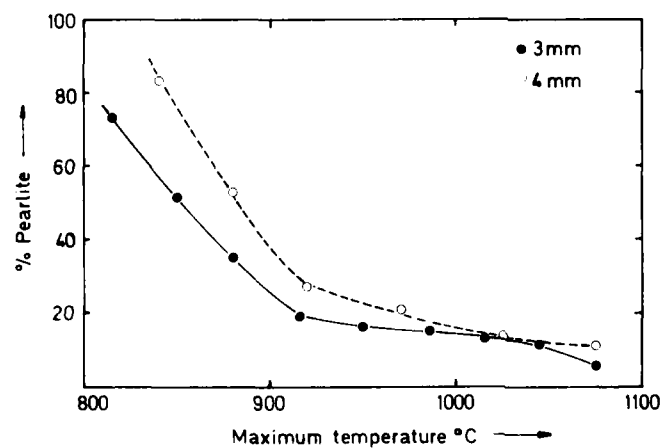the fusion zone.

Figure 64. The percentage of pearlite formed in the
weld simulator as a function of maximum
temperature reached for e and 4 mm thick
specimens.

61